

Surface-plasmon properties of noble metals with exotic phases

Okan K. Orhan¹ and Mauricio Ponga¹

¹*Department of Mechanical Engineering, University of British Columbia,
2054 - 6250 Applied Science Lane, Vancouver, BC, V6T 1Z4, Canada*

Noble-metal nanoparticles have been the industry standard for plasmonic applications due to their highly populated plasmon generations. Despite their remarkable plasmonic performance, their widespread use in plasmonic applications is commonly hindered due to limitations on the available laser sources and relatively low operating temperatures needed to retain mechanical strength in these materials. Motivated by recent experimental works, in which exotic hexagonal-closed-packed (HCP) phases have been identified in gold (Au), silver (Ag) and copper (Cu), we present the plasmonic performance of two HCP polytypes in these materials using high-accuracy first-principles simulations. The isolated HCP phases commonly reach thermal and mechanical stability at high temperatures due to monotonically decreasing Gibbs free energy differences compared to the face-centered cubic (FCC) phases. We find that several of these polytypes are harder and produce bulk plasmons at lower energies with comparable lifetimes than their conventional FCC counterparts. It also leads to the localized surface-plasmon resonance (LSPR) in perfectly spherical HCP-phased nanoparticles, embedded onto dielectric matrices, at substantially lower energies with comparable lifetimes to their FCC counterparts. LSPR peak locations and lifetimes can be tuned by controlling the operational temperature, the dielectric permittivity of hosting matrix and the grain size. Our work suggests that noble-metal nanoparticles can be tailored to develop exotic HCP phases to obtain novel plasmonic properties.

I. INTRODUCTION

Noble metal nanoparticles (NPs) and thin films are the most commonly used plasmonic media in diverse opto-electronic applications such as data recording [1–4], bio-sensing and imaging [5–9], photo-induced and heat-assisted drug delivery [10–13]. Most of these applications are commonly operated above room temperature (around ~ 300 – 400 K) where these metals tend to easily deform due to their relatively low stacking fault energy and high ductility [14]. There have been considerable efforts to improve the mechanical properties of noble-metal-based NPs while retaining or improving plasmonic properties with different strategies such as alloying [15–20]. However, substitutional alloying of noble metals commonly reduces plasmonic performance at the most common operational wavelengths [22, 29]. Therefore, the quest for finding novel materials capable of generating strong

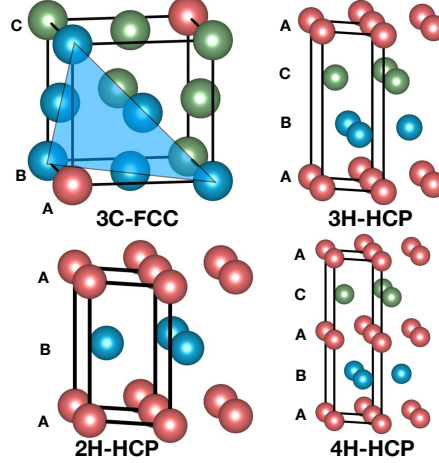


FIG. 1. Representative face-centered cubic structure (top-left) with the $\{111\}$ plane highlighted in blue. The 3H-hexagonal-closed-packed equivalent structure with the ABC stacking sequence (top-right). 2H-HCP and 4H-HCP polytypes are shown at the bottom left and right panels, respectively. The relative stacking of $\{111\}$ planes is also shown.

plasmons with significant lifetimes (in the order of ≥ 1 fs) and at lower energies remains an open challenge.

Noble metals such as Au, Ag and Cu most commonly appear in the face-centered cubic (FCC) phase which has a closed-packed atomic-plane arrangement of the ABC-stacking sequence along the $\{111\}$ crystallographic plane, as illustrated in Fig. 1. However, there has been a considerable effort to develop more exotic phases such 2H-HCP (AB-stacking sequence) and 4H-HCP (ABAC-stacking sequence) phases, illustrated in Fig. 1. Huang *et al.* has shown that Au-2H-HCP thin films can be grown on graphene oxide sheets [23], while Bian *et al.* has successfully produced Au-2H-HCP NPs in controlled-diffusion super-crystals [24]. Fan *et al.* has also synthesized FCC-2H-HCP-FCC hetero-phase nanoribbons [25]. Similarly, it has been shown that the Au-4H-HCP polytype can be stabilized into nanoribbons [26] and metastable nanorods [27]. Benaissa and Ferhat [28] have demonstrated that 2H-, 4H-, and 6H-HCP Au phases can be thermally and dynamically can be stabilized using first-principles methods.

Chakraborty *et al.* have managed to grow the meta-stable thick films of Ag-4H-HCP and two-dimensional Ag-2H-HCP using the controlled electrochemical deposition on the silicon and glass substrates [29]. They have also shown that the 4H-HCP phase is relatively stable using the first-principles simulations. Recent experimental work carried out by Thevamaran *et al.* have shown that the 2H-HCP and 4H-HCP phases of Ag can be achieved by a simultaneous martensitic phase transformation when Ag micro-particles are impacted onto an obstacle at a high velocity using laser-induced projectile impact test (LIPIT) [30, 31]. This martensitic phase transformation has

been further corroborated by Funes *et al.* [32]. In these works, Ag NPs formed gradient nano-grained (GNG) structures [33] due to a decaying shock pressure providing a vast domain of rich microstructures to engineer material properties. Other works have documented Ag with HCP structure, in particular when extracted from Ag/Au ores of north Russia, when synthesized using a high-pressure magnetron, in nanorods (diameter $\sim 10\text{--}100\text{ nm}$), nanoribbons, and bulk films [34–36]. Moreover, using solution-phase epitaxial growth under ambient conditions, 4H hexagonal Cu was grown on 4H Au nanoribbons [26]. This epitaxial growth was also extended to other materials such as Ir, Rh, Os, Ru as well [37].

However, plasmonic properties of such architected materials with HCP-based polytypes remain unavailable since it is relatively difficult to synthesize these polytypes. This issue hinders the experimental characterization of such materials for plasmonic properties. Fan *et al.* has performed the monochromated electron-energy loss spectroscopy (EELS) measurements on the thin 2H-HCP and 4H-HCP Au nanoribbons and calculated the dielectric functions within a semi-empirical approach [25, 26]. In that work, they have used the experimentally available data for the FCC Au to describe the low-energy spectral range. Bian *et al.* [] has predicted a localized surface plasmon resonance (LSPR) of the Au-2H-HCP super-crystals in the ordered arrays and found a strong plasmonic peak at $\sim 630\text{ nm}$ ($\sim 1.97\text{ eV}$)[24].

We herein present a systematic and comprehensive study of the stability assessment and temperature-dependent material properties of the 2H-HCP and 4H-HCP phases of Au, Ag and Cu within the fully first-principles approaches. We first investigate the thermal and mechanical stabilities of the isolated HCP crystals using density-functional theory (DFT) [38, 39] and its perturbative extension called the density-functional perturbation theory (DFPT) [40, 41]. It is shown that the underlying KS band-structure is not sufficiently well-defined when the random-phase approximation (RPA) [14–17] is used to describe the inter-band transitions in noble metals. The G_0W_0 [29, 31, 46] method is applied to obtain the approximate quasi-particle (QP) band-structures [48–50] to improve accuracy of the optical simulations. The intra-band part, also called the Drude plasmon, is included in the Drude-Lorentz model [51–54] using the first-principles temperature-dependent plasmonic parameters.

Inspired by these recent experimental works on stabilizing NPs of the exotic noble-metal phases, we analyze the LSPR in perfectly spherical NPs of 2H-HCP and 4H-HCP phases embedded onto a dielectric substrate such as silica and compare them to the FCC phase. The effects of hosting matrix and NP size are analyzed. An operational wavelength and temperature of 830 nm and 400 K are chosen as they are the most common operational condition in the emerging heat-assisted

magnetic recording (HAMR) [1, 4, 55] where the high-power near-field-transducer (NFT) [55–57] is used as the plasmonic antenna to achieve temporary and instant heating of a local region in the recording medium above its Curie temperature. The current NFT designs are mainly based on the FCC Au, which is soft and may protrude or deform for temperature rises as little as a few tens of Kelvin [14]. We investigate the thermal and mechanical properties of the HCP-based polytypes to assess their relative performance compared to the FCC Au.

The discoveries mentioned above and technologically relevant problems are the motivation behind this work. However, beyond that, this work provides a well-defined workflow and practical computational experiments for plasmonic materials. A comprehensive Supplementary Information (SI) is available for the readers to provide a thorough background on the electronic structure, theoretical spectroscopy, thermal and mechanical properties of metallic solids, and further data analysis on the 100 – 500 K temperature range.

II. THEORETICAL AND COMPUTATIONAL METHODS

In this section, we introduce the theoretical concepts, their computational implementations and limitations. A schematic illustration of the workflow used for the first-principle simulations is presented in Fig. 2.

Kohn-Sham DFT (KS-DFT) [38, 39] using semi-local electronic exchange-correlation (xc-) functionals [39, 58–60] is an almost-ubiquitous approach for simulating ground-state properties of

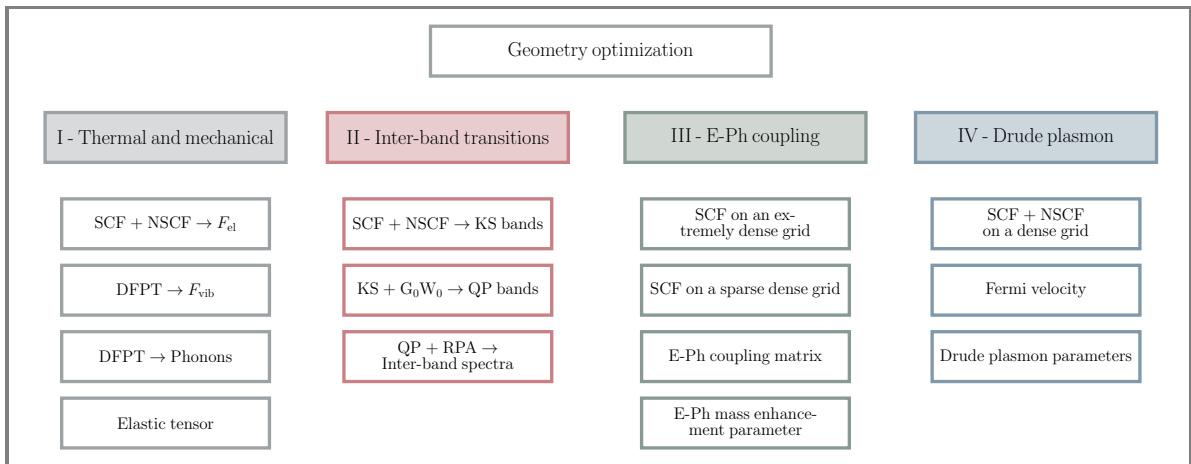


FIG. 2. The schematic illustration of workflow used for the first-principle simulations. SCF: Self-consistent field, NSCF: Non-SCF, F_{el} : Electronic Helmholtz free energy, F_{vib} : Vibrational Helmholtz free energy, DFPT: Density-functional perturbation theory, E-Ph: Electron-phonon, KS: Kohn-Sham, QP: Quasi-particle

solids. It also offers a computationally feasible framework to obtain the second-order elastic tensor within Hooke's law and the lattice dynamics within the density-functional perturbation theory (DFPT) [40, 41]. It also provides a computationally feasible starting point for theoretical spectroscopy simulations such the random-phase approximation (RPA) [14–17].

A. Figures of merits for stability assessment

Three stability assessments are necessary to ensure stability of the HCP-based structures. It is important to note that the stability assessment of the HCP phases are performed for the isolated phases. Commonly, they have been grown within complex hetero-phased structures for which the thermal and mechanical stability is achieved through complex mechanisms beyond the scope of this work.

For the sake of a direct comparability, we alternatively use a HCP unit cell with the ABC-stacking sequence to represent FCC phase, as shown in Fig. 1. This FCC-equivalent phase is conveniently called 3H-HCP to achieve a more systematic and simplified notation throughout this work. To ensure that the 3H-HCP unit cell are structurally equivalent to the FCC unit cell, the corresponding structural parameters of their relaxed geometries are compared in Table S1. The percentage relative differences are $\leq 1\%$ for the lattice parameters and the angle between A-B-C atoms in Fig. 1. The first line of the stability assessment is the thermal stability. The Gibbs free energy (GFE) is commonly used as the figure of merit (FOM) to assess formation of the competing phases in a solid. Using the GFE of 3H-HCP phases as the reference systems, the relative GFEs of the HCP-based phases are evaluated by $\Delta G = G^{n\text{H-HCP}} - G^{3\text{H-HCP}}$ where $n = 2, 4$ (see SI for a brief summary of GFE of a non-magnetic, elemental pristine solid). The second line is the elastic-stability assessment which is evaluated according to the Born-Huang-stability criteria [61](see SI for further details). These criteria are indeed a special case of the thermal stability condition ensuring that the GFE of an unstrained crystal is a minimum compared to any other states achieved by infinitesimal strains [62]. Otherwise, there is a high possibility of phase transformation to a lower symmetry. Finally, the dynamics-stability assessment is evaluated by analyzing phonon dispersions. An unstressed crystal is expected to have only real (positive) phonon modes. Harder phonon modes (higher frequencies) indicate superior dynamical stability as softer phonon modes signal possible phase transitions to lower symmetry structures at a finite temperature [63]. The necessary quantities are calculated through the first column in Fig. 2.

B. Optical and plasmonic properties

At the low-energy spectral range, the optical response of metallic solids is almost entirely electronic and due to two main physical phenomena, namely the inter-band and intra-band transitions, which can be symbolically expressed via the macroscopic complex dielectric function given by $\mathcal{E}(\omega) = \mathcal{E}^{\text{inter}}(\omega) + \mathcal{E}^{\text{intra}}(\omega) = \mathcal{E}_1(\omega) + i\mathcal{E}_2(\omega)$. The macroscopic complex dielectric function often serves as the central optical function due to its well-established analytical connections with optical measurements.

The inter-band transitions are due to the vertical transitions of electrons between the occupied and unoccupied electronic states. This part can be perturbatively calculated using RPA build on the highly well-defined single-particle electronic states (see SI for further details). It has been shown that RPA fails to accurately describe the inter-band transitions in Au, Ag, and Cu [29]. This is due to the missing electron-hole quasiparticle (QP) screening within the approximate KS-DFT [48–50], leading to an inadequate description of the fully filled *d*-bands of bulk Au, Ag, and Cu [29, 31, 64]. The most common corrective approach to improve the accuracy of underlying electronic structures is to use the QP formalism [65, 66] due to its high compatibility with the approximate KS-DFT (see SI for further details). Within this formalism, the inter-band transitions are obtained through the second column in Fig. 2.

The intra-band transition, also called *the Drude plasmon*, is due to the collective oscillations of the nearly free electrons in phase with the longitudinal part of the driving electromagnetic radiation. Unlike the inter-band transition simulations, it requires a highly dense Brillouin zone sampling at and around the Fermi surface, i.e., at least around ~ 16000 grid points [67], which is not feasible for high-throughput simulations. Thus, the Drude plasmon is classically treated within the Drude-Lorentz model given by [51–54]

$$\mathcal{E}^{\text{intra}}(\omega) = 1 - \frac{\omega_p^2}{\omega^2 + i\eta_p\omega}, \quad (1)$$

where ω_p and η_p are the Drude plasmon energy (plasma frequency) and the inverse lifetime, respectively. The Drude plasmon energy is approximately given by

$$\omega_p^2 = \frac{4\pi}{3}N(E_F)\langle v_F^2 \rangle, \quad (2)$$

where $N(E_F)$ and v_F are the density-of-state (DOS) at the Fermi level and the Fermi velocity, respectively. Within Matthiessen’s rule, the inverse lifetime for a *pristine* solid can be expressed

as the sum of the electron-electron (e-e) and the electron-phonon (e-ph) scatterings terms given by

$$\eta_{\text{p}} = \eta_{\text{e-e}} + \eta_{\text{e-ph}}. \quad (3)$$

In general, the e-ph scattering is the predominant phenomenon; however, the e-e scattering is still relatively significant for noble metals compared to other metals [68]. The e-e scattering contribution to the inverse lifetime can be approximated within the Fermi liquid theory at the absolute-zero temperature by the expression (in the Hz unit) [69–71]

$$\eta_{\text{e-e}} = \frac{me^4(E - E_{\text{F}})^2}{64\pi^3\hbar^3\epsilon_0 E_s^{3/2} E_{\text{F}}^{1/2}} \left(\frac{2\sqrt{E_s E_{\text{F}}}}{4E_{\text{F}} + E_s} + \arctan \sqrt{\frac{4E_{\text{F}}}{E_s}} \right), \quad (4)$$

where m , e , \hbar , and ϵ_0 are the electronic mass, the unit charge, the reduced Plank constant and the vacuum permittivity, respectively. E_s is the kinetic energy associated with the Thomas-Fermi screening length $q_s = e\sqrt{N(E_{\text{F}})/\epsilon_0}$ given by $E_s = \hbar^2 q_s^2 / (2m)$. This term accounts for the scattering of electrons around the Fermi level. Hence, $(E - E_{\text{F}})$ is consistently set to represent the smearing parameter used for the double-delta integral during the e-ph coupling simulations. Within the Debye model, the e-ph scattering term is approximately given by [72, 73]

$$\eta_{\text{e-ph}} = \frac{2\pi k_{\text{B}} \lambda T}{3}, \quad (5)$$

where T is the absolute temperature, and λ is the e-ph mass enhancement parameter. We refer the reader to Refs. 73 and 74 for details on how to obtain the e-ph mass enhancement parameter using DFPT, summarized in the third column in Fig. 2.

Assuming that the metallic bands have a parabolic dispersion normal to the Fermi surface, the averaged Fermi-velocity square in Eq. (2) is approximated by [75]

$$\langle v^2(E_{\text{F}}) \rangle = \frac{\left(\sum_i \int_{S_{\text{F}_i}} d\mathbf{k} \left| \frac{\partial E_{i,\mathbf{k}}}{\partial \mathbf{k}} \right|^2 \right)}{\left(\sum_j \int_{S_{\text{F}_j}} d\mathbf{k}' \right)}, \quad (6)$$

where S_{F_i} and $E_{i,\mathbf{k}}$ are the Fermi surface and the KS energy of the i -th metallic band, respectively. The average of the Fermi-velocity square is practically evaluated on a slab with a thickness of d_{Fermi} . In principle, at the absolute zero, $d_{\text{Fermi}} \rightarrow 0$; however, at a finite temperature, the Fermi surface is smeared due to excitation of electrons close to the Fermi surface. The finite-temperature effect can be carried to the average of the Fermi-velocity square by setting $d_{\text{Fermi}} = k_{\text{B}}T$ representing

the electronic temperature. By doing so, the average of the Fermi-velocity becomes consistent with the inverse plasmon lifetime given by Eq. (4) and Eq. (5). Furthermore, the Fermi velocity is re-normalized by λ and becomes $v_F \rightarrow v_F/(1 + \lambda)$ [76]. The final Drude parameters are obtained by the fourth column in Fig. 2.

C. Localized surface-plasmon generation in the perfectly spherical nanoparticles

The condition of the LSPR generation in a metallic NP smaller than the incident wavelength and embedded onto a dielectric hosting matrix is given by [77].

$$\mathcal{E}_1 = -2\mathcal{E}_m, \quad (7)$$

where \mathcal{E}_1 is the real part of the bulk macroscopic dielectric function of the metallic NP and \mathcal{E}_m is the dielectric permittivity of the hosting matrix. By this condition, the LSPR of a metallic NP becomes [78]

$$\omega_{\text{sp}} = \sqrt{\frac{\omega_p^2}{1 + 2\mathcal{E}_m + \mathcal{E}_1^{\text{inter}}} - \eta^2}, \quad (8)$$

where η is the inverse lifetime of the LSP generated on the NP. This constant can be given for an arbitrarily shaped NP given by [79, 80]

$$\eta = \eta_p + \alpha \frac{v_F}{L_{\text{eff}}}. \quad (9)$$

$L_{\text{eff}} = 4V/A$ is the effective path length of hot carriers [79] where V and A are the volume and the surface of the NP, respectively. α is the theory-dependent constant which is in the order of 1.

D. Figures of merits for mechanical properties

In addition to high plasmonic performance, it is crucial for a candidate plasmonic to have good workability for easy integration in any design, mechanical strength, and hardness for durability. Mechanical properties of complex materials such as the GNG structure are determined by a large number of parameters such as grain-boundary energies, grain sizes and gradient [81–83]. Despite that, the elastic constant of a perfect crystal can provide an initial assessment of its mechanical performance. Three simple FOMs can be used to assess workability, strength, and hardness, i.e.,

Poisson's ratio, Pugh ratio (ratio between bulk and shear moduli), and hardness. Commonly, a critical minimum-value (CMV) of 0.25 for Poisson's ratio [84] and a CMV of 1.75 for the Pugh ratio [85] are expected for materials with large plastic deformation and ductility, respectively. The final FOM is the Vickers hardness (H_V), which can be used as a measure for the yield strength (σ_y) since they are approximately related by $H_V \approx 3 \sigma_y$ [86]. H_V is commonly approximated by its semi-empirical relation to the shear modulus (S) by $H_V^{\text{Teter}} = 0.151S$ [87].

E. Approximate thermal conductivity

During the high-power NFT operations, the feedback heat has to be quickly dissipated to avoid excessive thermal softening and plastic deformation [55]. High thermal conductivity is desirable to endure high operational temperatures. Free electrons in metals are the main mediator for heat conduction. The electronic thermal conductivity can be approximated by substituting the electronic conductivity (σ) within the Drude model into the Wiedemann-Franz law (including the quantum effects), given by

$$\begin{aligned} \kappa_e &= \frac{\pi^2 k_B^2 T \sigma}{3e^2}, \quad \text{where} \quad \sigma = \frac{2e^2}{3} \frac{N(E_F)}{V_0} \frac{\langle v_F^2 \rangle}{(1+\lambda)^2} \eta_p^{-1} \Rightarrow \\ \kappa_e &= \frac{2\pi^2 k_B^2 T}{9} \frac{N(E_F)}{V_0} \frac{\langle v_F^2 \rangle}{(1+\lambda)^2} \eta_p^{-1}, \end{aligned} \quad (10)$$

where V_0 is the equilibrium volume and 2 accounts for the spin-channels.

Second significant mediator of the heat conduction above the Debye temperature is the lattice thermal conductivity mediated via phonons. It is given by the semi-empirical formula [88]

$$\kappa_{\text{lat}} = f(\gamma) \frac{m_{\text{avr}} V_0^{1/3} \Theta_D^3}{\gamma N^{2/3} T}, \quad (11)$$

where m_{avr} , N , Θ_D , and γ are the average mass, the number of atoms, the Debye temperature, and the Grüneisen parameter, respectively (see SI for further details). Finally, the scaling function is given by

$$f(\gamma) = \frac{2.42814 \times 10^7}{1 + 0.228/\gamma^2 - 0.514/\gamma}, \quad (12)$$

when m_{avr} in (kg) unit and V_0 in (m^3) unit for κ_{lat} in ($\text{W} \cdot \text{m}^{-1} \cdot \text{K}^{-1}$) unit.

III. RESULT AND DISCUSSION

A. Stability assessment

We start with the stability assessment of the isolated crystals. In Fig. 3, the GFE differences (ΔG) of the 2H-HCP and 4H-HCP phases with respect to the 3H-HCP counterparts are shown for $T = 400$ K. At this operational temperature, the 2H-HCP and 4H-HCP phases are thermally less favorable. However, their ΔG is in the order of 1 meV except for Au-2H-HCP. This small difference (1 meV) is nearly the numerical accuracy of the KS-DFT. Hence, those with a ΔG in this order are pretty likely to be thermally stabilized through an appropriate manufacturing process via residual stresses. One example can be the case of HCP-based Ag phases [30–32] stabilized via the severe plastic deformation or controlled electrochemical deposition [29]. General trends in ΔG are predominantly determined by the vibrational Helmholtz free-energy differences (ΔF_{vib}), while the electronic contribution (ΔF_{el}) are negligible (see Fig. S1 for temperature-dependent free-energy differences). Except for Au-2H-HCP, ΔF_{vib} monotonically decreases with increasing temperature due to the entropic contributions. This leads to thermal stabilization of Ag-2H-HCP, Ag-4H-HCP, Cu-2H-HCP, and Cu-4H-HCP at 853 K, 745 K, 1350 K and 1125 K, respectively. The isolated Au-4H-HCP is expected to melt before reaching thermal stability as its ΔG becomes negative at an extreme temperature when extrapolated.

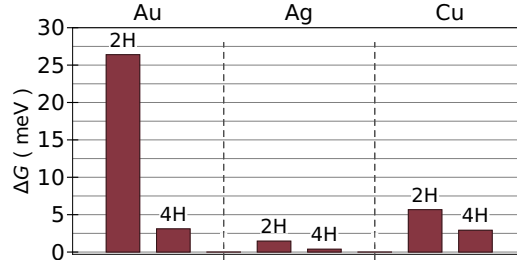


FIG. 3. Gibbs free-energy differences per atom ($\Delta G = \Delta E_0 + \Delta F_{\text{el}} + \Delta F_{\text{vib}}$) of the isolated 2H-HCP and 4H-HCP phases of Au, Ag and Cu with respect to their FCC-equivalent 3H-HCP phases at 400 K.

Finally, the phonon dispersions of the studied noble metal polytypes show positive (real) phonon modes, indicating dynamical stability at the absolute zero temperature (see Fig. S2 for phonon dispersions). There is an incomplete phonon softening between $\Gamma \rightarrow A$ in the Au-3H-HCP phase, which can be a precursor for a martensitic phase transformation [89]. Similarly, the Ag-2H-HCP and the Ag-3H-HCP phases also exhibit incomplete phonon softening between $\Gamma \rightarrow A$, unlike the Ag-4H-HCP phase. This softening is possibly indicating superior dynamical stability in the Ag-4H-

HCP phase. The Cu polytypes do not have any softening phonon modes, and the general trend is softer phonon modes (lower phonon frequencies) following an increasing trend from 2H-HCP \rightarrow 3H-HCP \rightarrow 4H-HCP.

B. Bulk optical and plasmonic response

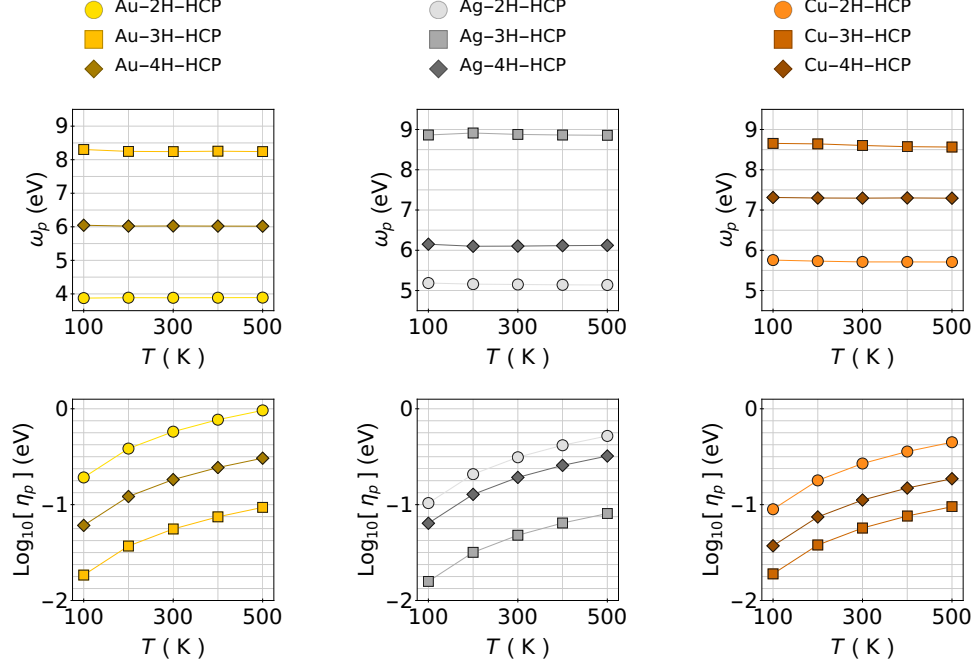


FIG. 4. Temperature-dependence of the Drude plasmon energy and the inverse lifetime of the isolated Au, Ag and Cu polytypes.

In Fig. 4, the temperature-dependence of the Drude plasmon energies (ω_p) and inverse lifetimes (η_p) are shown. These values are also listed in Table S3. For any given polytype, ω_p has a subtle temperature-dependence due to the similar temperature-dependence of its Fermi velocity, v_F (see Fig. S3 for the temperature-dependence of v_F). On the other hand, the inverse lifetime (η_p) is linearly increasing with the increasing temperature due to the almost-linear temperature-dependence of η_{e-ph} in Eq. (5). The e-e term (η_{e-e}) generally has an exponentially increasing trend with the increasing temperature; however, this term is in the order of $10^{-4} - 10^{-3}$ eV. Drude plasmon energies follow an ordering of $\omega_p^{3H} > \omega_p^{4H} > \omega_p^{2H}$, while the inverse lifetimes have an opposite trend. The ordering of ω_p among the polytypes of a given metal follows the ordering of v_F . Since $\omega_p \propto \sqrt{N(E_F)}/\lambda$, the identical orderings in DOS and λ almost balance themselves (see Fig. S3). The ordering in v_F (so in ω_p) is due to the steeper band dispersion in the 3H-HCP

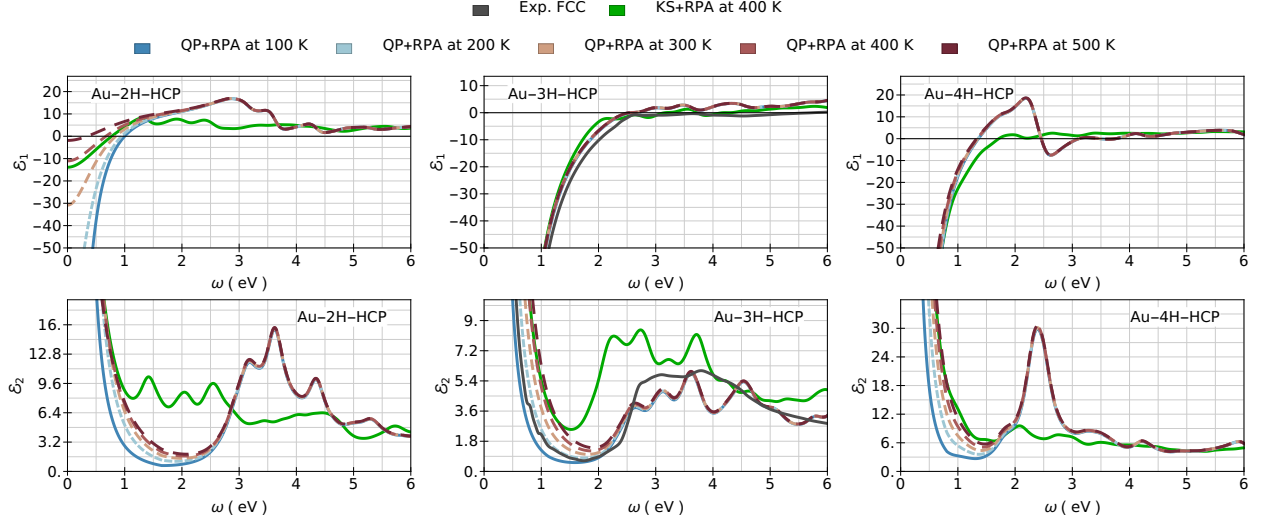


FIG. 5. Temperature dependence of the macroscopic dielectric functions of Au polytypes, calculated using the random-phase approximation build on the quasi-particle band-structures (QP+RPA). The macroscopic dielectric functions build on the Kohn-Sham band-structures (KS+RPA) at 400 K are shown for comparison. The experimentally available data for the FCC phase were extracted from Ref. 90.

polytypes.

The calculated Drude plasmon energies (listed in Table S3) of the 3H-HCP phases are between 8.0 – 9.0 eV, which are in close agreement with the previous experimental and theoretical works ranging between $\sim 7.5 - 9.5$ eV. We refer the reader to Ref. 29 for further details. The Au-2H-HCP phase produces the Drude plasmon at a very low energy, i.e., ~ 3.8 eV. However, it is a relatively short-living with a 7.17 fs lifetime at the room temperature (listed in Table S3). The other HCP-based polytypes also produce Drude plasmons at lower energies compared to their FCC counterparts. This result is quite promising as these polytypes may give much lower energies (higher frequencies) to generate bulk plasmons and enable more diverse applications. For instance, heat-assisted magnetic recording devices commonly use 830 nm wavelength at the higher temperatures [22], while most medical and bio-sensing applications use the typical red laser (~ 650 nm) at lower temperatures [29].

In Figs. 5 - 7, the macroscopic dielectric functions within RPA starting from the KS band-structures (KS+RPA) for 400 K and the QP band-structures for 100–500 K are presented alongside the available experimental spectra for the 3H-HCP phase, extracted from Ref. 90. The temperature dependence of the Drude plasmons predominantly affects the near-infrared spectral range of the absorption spectrum where $\mathcal{E}_2 \approx \omega_p^2 \eta_p / (\omega^3 + \omega \eta_p^2)$. Hence, it is scaled by η_p which has a strong temperature-dependence. The real part, \mathcal{E}_1 has a more subtle temperature dependence due to $\mathcal{E}_1 \approx 1 - \omega_p / (\omega^2 + \eta_p^2)$ where η_p -dependence rapidly vanishes for the increasing ω . This is due

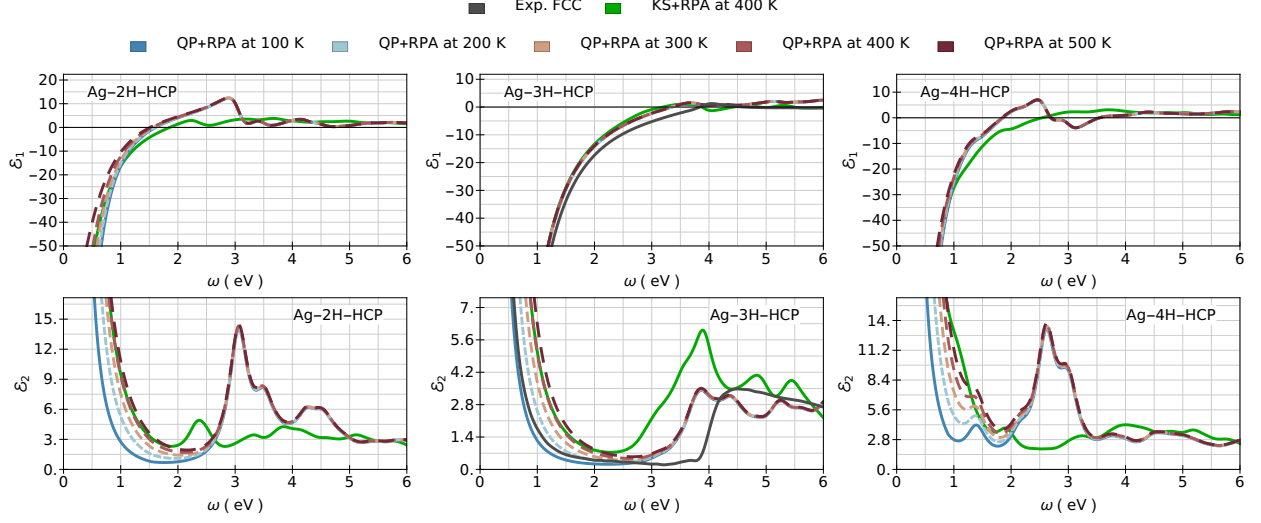


FIG. 6. Temperature dependence of the macroscopic dielectric functions of Ag polytypes, calculated using the random-phase approximation build on the quasi-particle band-structures (QP+RPA). The macroscopic dielectric functions build on the Kohn-Sham band-structures (KS+RPA) at 400 K are shown for comparison. The experimentally available data for the FCC phase were extracted from Ref. 90.

to the fact that $\mathcal{E}_2 = \omega_p^2 \eta_p / (\omega^3 + \omega \eta_p^2)$, which is scaled by η_p . The only exception is the Au-2H-HCP phase for which the asymptotic tail at 0 K becomes finite for $\omega \rightarrow 0$ with the increasing temperature. This is due to the fact that its η_p is converging to the order of ω_p and $\mathcal{E}_1 = 1 - \omega_p^2 / \eta_p^2$ for $\omega \rightarrow 0$.

Figs. 5 - 7 show the dielectric functions for the three polytypes as computed by the QP+RPA,

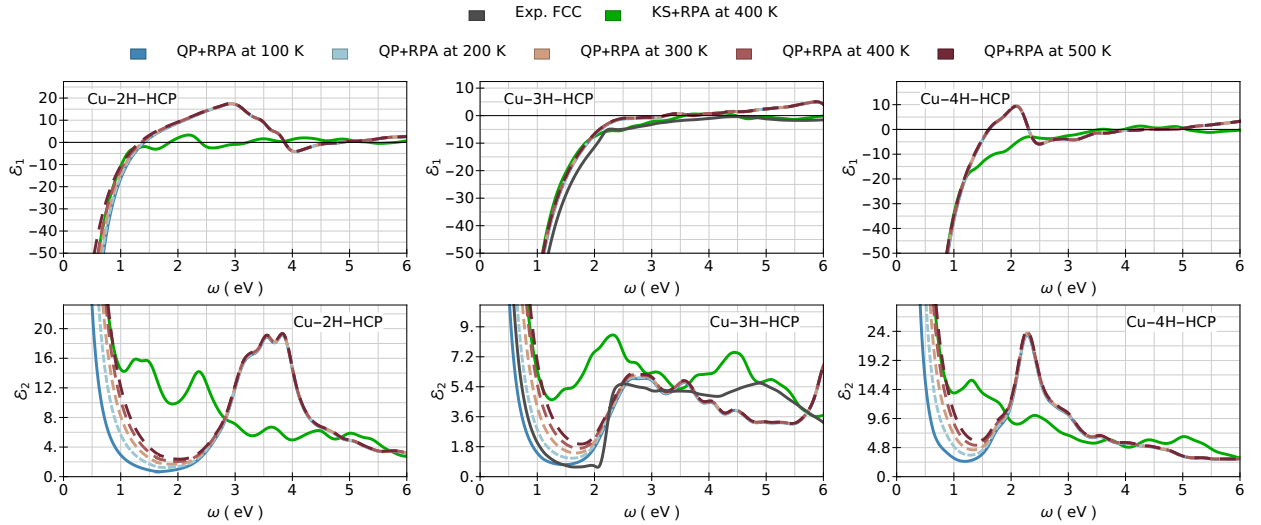


FIG. 7. Temperature dependence of the macroscopic dielectric functions of Cu polytypes, calculated using the random-phase approximation build on the quasi-particle band-structures (QP+RPA). The macroscopic dielectric functions build on the Kohn-Sham band-structures (KS+RPA) at 400 K are shown for comparison. The experimentally available data for the FCC phase were extracted from Ref. 90.

and the KS-RPA. For the cases of the 3H-HCP (shown in the middle top and bottom panels of Figs. 5 - 7), experimental values of the dielectric function are also provided. It can be observed that the dielectric functions of the 3H-HCP phases within the QP+RPA are in good agreement with the experimental absorption spectra. In particular, the Drude tails match the experimental curves nicely at around $\sim 100 - 200$ K and the predicted QP+RPA captures most of the trends observed in experiments. Some discrepancies are evident, in particular, where the Drude tails merge to the inter-band parts. The experimental curves in Ref. 90 are indeed obtained by combining the different experimental data from Ref. 91 as it is not feasible to obtain the entire spectral range within a single experiment. For instance, the low-energy spectral range and the inter-band transitions were separately obtained and later combined [90]. Hence, there are discontinuities where the intra-band and inter-band parts merge in the experimental curves. These also explain the sharper inter-band transition edges in the experimental curves compared to the more smeared edges in our calculated spectra. Despite that, the QP+RPA successfully predicted the low-energy spectral range while capturing the trends of the different experimental approaches at high-energy ranges. For instance, for Au at $\omega = 2$ eV, QP+RPA predicts $\mathcal{E}_1 = -6.9$ and $\mathcal{E}_2 = 0.82$ while the experimental values are $\mathcal{E}_1 = -10.3$ and $\mathcal{E}_2 = 0.87$ at 100 K. The discrepancy is much higher within KS+RPA as it predicts $\mathcal{E}_1 = -3.6$ and $\mathcal{E}_2 = 5.0$. Similar behavior can be seen for Ag and Cu, as shown in Figs. 6 - 7 middle panels. It is also important to note that the experimental Drude plasmon parameters substantially vary in the literature. We refer to the reader Refs. 90 and 29 for a more comprehensive discussion on the experimental measurements of the Drude plasmons for the FCC phases.

There are also some discrepancies at the higher energies where only the inter-band transitions occur. It is important to note that the experimental spectra tend to be more smeared due to the experimental conditions and the defects in samples. In the calculations, we use a fixed value of 0.2 eV for the inverse lifetime of the inter-band transitions rather than larger smearing to have a better resolution. Despite these discrepancies, the QP+RPA trends are in line with the experiments, while the KS+RPA spectra are substantially more inaccurate.

Having gain confidence in the absorption spectra predictions using the QP+RPA, we now focus on comparing the absorption spectra within KS+RPA and QP+RPA, as shown in the bottom panels of Figs. 5 - 7. Different trends can be observed for the macroscopic dielectric function due to the G_0W_0 correction. For the 2H-HCP and 4H-HCP phases, the absorption peaks are located at higher energies with considerably high intensities within QP+RPA compared to the KS+RPA. This is due to two main effects of the G_0W_0 correction on the underlying electronic bands (see Fig. S4 for the KS and QP band-structures). The first effect is that the G_0W_0 correction steepens

the band dispersion. As the exchange part of the self-energy is only effective on the valence bands, the average stretching is larger on the valence bands compared to the conduction bands. This shifts the absorption peaks to higher energies. The second effect is that a total shift of the d -band centers to higher energies. This migrates the higher energy peaks to lower energies, contributing to the intense absorption peaks in the 2H-HCP and 4H-HCP phases. In the 3H-HCP phases, the first effect is also present; however, the d -band centers are not substantially shifted. It leads to the total shifts in their absorption spectra to higher energies with less intensity. The shift is not fully sufficient in the Ag-3H-HCP case for which QP+RPA slightly underestimates the absorption-spectrum edge compared to the experimental spectrum, as can be observed in Fig. 6 in the middle bottom panel. This partial discrepancy can be due to the missing spin-orbit coupling in our work as G_0W_0 and the phonon dispersion simulations lack spin-orbit coupling. By all means, it is far more complex as the quantum many-body effects due to both electrons and excitations play significant roles.

Despite being purely a bulk property, the dielectric function determines the LSPR population. It sets crucial preliminary conditions for LSPR for which $\mathcal{E}_1 \approx -1$ and $\mathcal{E}_2 \approx 0$ need to be satisfied [92]. The first condition is to ensure sufficient free electron density, while the second condition is to avoid a high electron-hole-pair population. With these conditions in mind, the 2H-HCP phases, followed by the 4H-HCP, satisfy the first condition at lower energies than the 3H-HCP phases. In particular, the \mathcal{E}_1 of Au-2H-HCP polytype approaches to first-instance where $\mathcal{E}_1 \approx -1$ at a quite-low energy of ~ 0.6 eV. This predicts a high LSP generation at lower energies; however, $\mathcal{E}_2 \gg 0$ indicating a rapid decay to electron-hole-pair. Furthermore, \mathcal{E}_2 of the 2H-HCP and 4H-HCP phases becomes quite large at higher energies than the 3H-HCP phases indicating shorter-living LSPR despite the enhanced intensity. The only exception is the Cu-4H-HCP, where \mathcal{E}_2 approaches its local minimum around when $\mathcal{E}_1 \approx -1$ where it may produce similar LSP generated by the Cu-3H-HCP. In summary, the overall shifted trend in the 2H-HCP and 4H-HCP phases indicates more intense LSPR where higher absorption intensities at these lower energies imply shorter-living ones.

C. Localized surface-plasmon generation in the perfectly spherical nanoparticles

We now turn our attention to the case where perfectly spherical NPs are embedded onto a dielectric hosting matrix such as silica. We point out that this problem definition is a very simplistic scenario, as the hosting matrix does not strongly interacts with the NPs.

In Fig. 8, LSPR in the spherical NPs with $R = 20$ nm embedded onto a representative dielectric

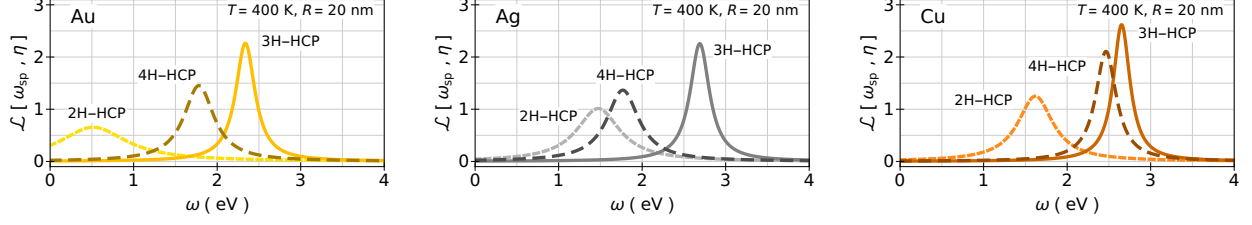


FIG. 8. Localized surface-plasmon resonance in the spherical nanoparticles of the noble-metal polytypes with radii of $R = 20$ nm at $T = 400$ K, shown using the Lorentzian line shape. The NPs are embedded onto a hosting matrix with a dielectric permittivity of $\mathcal{E}_m = 4$.

hosting matrix are shown at an operating temperature of $T = 400$ K, using the Lorentzian line shape denoted by $\mathcal{L}[\omega_{\text{sp}}, \eta]$ (also listed in Table S4). The dielectric permittivity of the representative dielectric hosting matrix is chosen as $\mathcal{E}_m = 4.0$ since it is approximately equal to the dielectric constant of silica [93]. The 2H-HCP-phased NPs have LSPR peaks at the lowest energies compared to their 3H-HCP and 4H-HCP counterparts. The LSPR peak of the Au-2H-HCP-phased NP is at a very low energy of ~ 0.90 eV with the shortest lifetime of 4.25 fs. The considerable short lifetime is mostly due to the strong e-ph coupling in Au-2H-HCP, indicating mainly rapid-decaying of LSPR to lattice vibrations. Moreover, the absorption-spectrum edge of Au-2H-HCP in Fig. 5 also hints a rapid-decaying of plasma into the electron-hole pairs. The Ag-2H-HCP NP generates LSPR at the closest energy of 1.63 eV with a lifetime of 6.58 fs with respect to the operational wavelength of 830 nm (~ 1.494 eV). The low-energy LSPR peaks in the 2H-HCP-phased NPs are primarily due to the strong e-ph mass enhancement parameters of the 2H-HCP phase which re-normalize the Fermi velocities and lead to the lower Drude plasmon energies as shown in Fig. 4.

The 4H-HCP-phased NPs have their LSPR peaks at higher energies compared to their 2H-HCP-phased counterparts while at lower energies compared to their 3H-HCP counterparts. The general trend in the LSPR energies is an increasing order of $\omega_{\text{sp}}^{3\text{H-HCP}} > \omega_{\text{sp}}^{4\text{H-HCP}} > \omega_{\text{sp}}^{2\text{H-HCP}}$. The LSPR lifetimes also follow a similar trend. In the case of Cu NPs, the 3H-HCP-phased and 4H-HCP-phased NPs generate LSPR peaks at the considerable close energies with comparable lifetimes of 13.68 *vs.* 17.00 fs, respectively.

The LSPR peak location and lifetime can be further tuned by controlling the operational temperature, the hosting matrix's dielectric permittivity and NP's size. In order to show these effects, we start by analyzing the temperature-dependence by setting $\mathcal{E}_m = 1.0$ in Eq. (8) and $\alpha = 0$ in Eq. (9). This setting eliminates the effects of the hosting matrix and the NP size, while the operational temperature is varied between 100 – 500 K as shown in Fig. S5. The increasing temperature shortens the plasmon lifetime due to $\tau_p \propto 1/T$ through Eq. (5). Moreover, it noticeably shifts the

LSPR peak to lower energies for the Au-2H-HCP, Au-3H-HCP and 4H-HCP phases, while for the remaining polytypes the effect is only minor.

Next, the operating temperature was set at 400 K to assess the effects of the hosting matrix by varying $\mathcal{E}_m = 1.0 - 2.0$ and the grain size by varying $R = 10 - 20$ nm as shown in Fig. S6. Increasing \mathcal{E}_m shifts the LSPR peaks to lower energies without having any effect on the lifetimes. Introducing the size effects by setting $\alpha = 1.0$ primarily lead to substantial shortening of the LSPR lifetimes. In the case of Au-2H-HCP-phased NP, it also shifts the LSPR peak to lower energies where such shift is higher for smaller NPs. Increasing NP size lengthens the LSPR lifetimes in all cases, since Eq. (9) is inversely proportional to the effective path length or simply to R for the perfectly spherical NPs. In summary, the increasing grains size has an opposite effect on the LSPR peaks compared to the increasing temperature and the increasing hosting-matrix dielectric permittivity.

D. Bulk mechanical properties

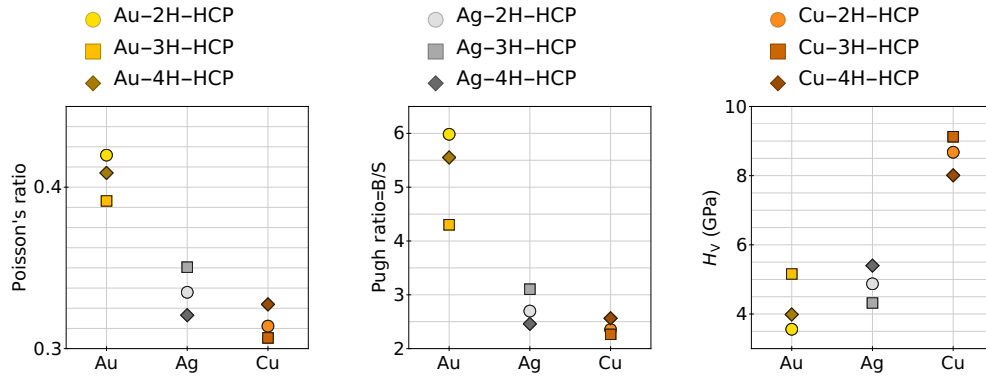


FIG. 9. Poisson's ratios, Pugh ratios and Vickers hardness for Au, Ag and Cu polytypes.

The mechanical FOMs are presented in Fig. 9. As expected, Au polytypes have the largest Poisson's and Pugh ratios, indicating a superior plastic deformation and ductility among all noble metal polytypes. However, these properties come at the expense of lowered hardness (H_V) and strength. It can be also seen when comparing their Vickers hardness to that of the Au-3H-HCP. Unlike Au, the 2H-HCP and 4H-HCP phases of Ag are predicted to have improved mechanical strength due to their lower Pugh ratios compared to the Ag-3H-HCP. Their Poisson's ratios above the CMV of 0.25 indicate that they also possess good workability. In terms of mechanical strength, the Cu polytypes have shown superior properties among the studied metals, i.e., low

Pugh ratio and high hardness. Although Cu-4H-HCP has the lowest Vickers hardness among the other Cu polytypes (~ 0.7 GPa, and ~ 1.1 GPa lower compared to the Cu-2H-HCP and Cu-3H-HCP, respectively), it has a much higher Vickers hardness compared to Ag and Au polytypes.

E. Approximate thermal conductivity

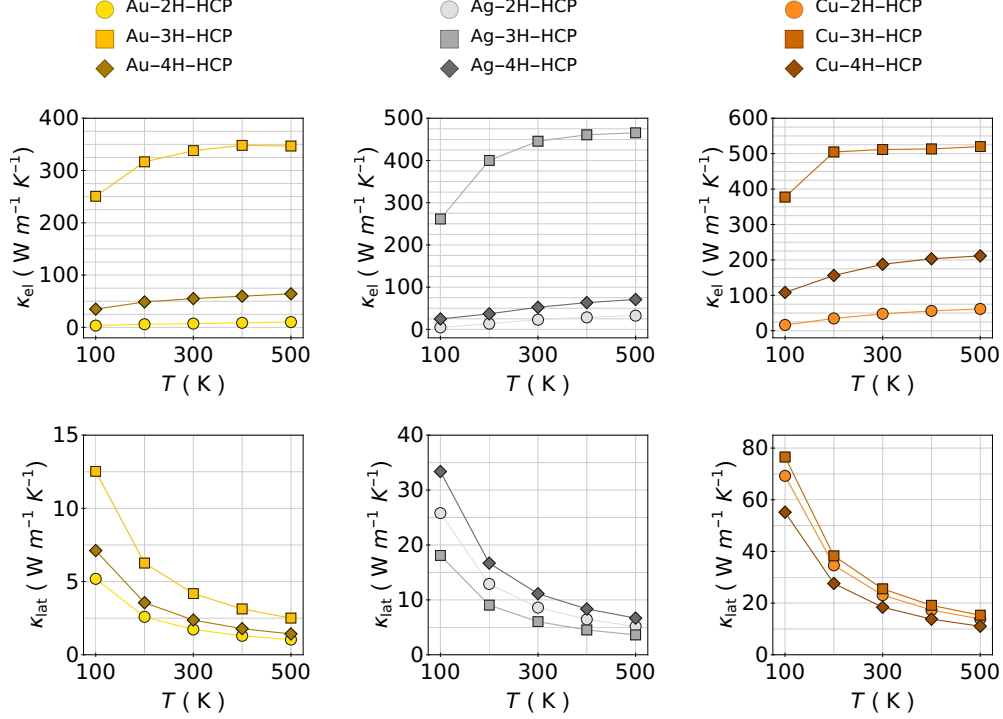


FIG. 10. Temperature-dependence of lattice (left panel) and electronic (right panel) thermal conductivity of the isolated bulk Au, Ag and Cu polytypes.

The temperature-dependent electronic and lattice thermal conductivities are shown in Fig. 10. The total thermal conductivities are also listed in Table S6. It is evident that the electronic conductivity is the most important contribution to thermal conductivity for all polytypes. The electronic conductivity shows an exponentially increasing trends with the increasing temperature due to its $T/(1 + \lambda)$ dependence in Eq. (10) where $N(E_F)$ and v_F are weakly temperature-dependent (see Fig. S3). On the other hand, lattice thermal conductivity exponentially decreases with temperature due to its $(1/T)$ dependence.

The total thermal conductivities of the Au-3H-HCP and Ag-3H-HCP are 351 and 465 ($\text{W} \cdot \text{m}^{-1} \cdot \text{K}^{-1}$) at 400 K, respectively. They are in reasonably good agreement with the experimental values 312 and 420 ($\text{W} \cdot \text{m}^{-1} \cdot \text{K}^{-1}$) [94] despite slight overestimation by our simulations. In the case of

the Cu-3H-HCP, the total thermal conductivity is $532 \text{ (W}\cdot\text{m}^{-1}\cdot\text{K}^{-1})$ which is quite overestimated compared to the experimental value of $392 \text{ (W}\cdot\text{m}^{-1}\cdot\text{K}^{-1})$ at 400 K [94]. Such overestimation is expected as we assume that our systems are perfect crystals. Hence, in Eq. (3), we do not include the electron-impurity scattering term, which can become significant above the room temperatures and reduce the plasmon lifetime, τ_p , depending on the sample [95]. Among all sources of error, τ_p is the most significant contributor to an overestimation of the thermal conductivity for Cu. It is worth mention Cu tends to quickly oxidize compared to the other noble metals, which can reduce the thermal conductivity significantly compared to the pristine metal.

In the case of 2H-HCP and 4H-HCP polytypes, the electronic thermal conductivity become much lower due to their large e-ph couplings which make difficult for the free electrons to mediate the heat dissipation.

IV. CONCLUSION

In this work, we have presented a comprehensive stability assessment and temperature-dependent material properties of 2H-HCP, 3H-HCP (FCC-equivalent) and 4H-HCP polytypes of Au, Ag and Cu. It has been found that the isolated 2H-HCP and 4H-HCP crystals become thermally more-favorable at high temperatures with respect to their 3H-HCP counterparts, with the exception of the Au-2H-HCP case. The isolated Au-2H-HCP crystal has a linearly increasing vibrational Helmholtz energy difference (ΔF_{vib}) with respect to the Au-3H-HCP phase. However, it is important to note that this phase has been stabilized in the hetero-phased nanoribbons. The studied polytypes successfully satisfy the elastic and dynamical stability criteria. The former one was demonstrated by applying the Born-Huang-stability criteria for the hexagonal symmetry, whilst the later one was assessed by analyzing the phonon dispersions which have positive phonon modes.

The increasing temperature has a very subtle effect on the Drude plasmon energy (ω_p) due to the weak temperature-dependence of the Fermi velocity (v_F) and the ratio $N(E_F)/(1 + \lambda)^2$ where $N(E_F)$ is the DOS at the Fermi level and λ is the e-ph mass enhancement parameter. On the contrary, the Drude plasmon inverse lifetime (η_p) is strongly temperature-dependent as $\eta_p \propto T$ via Eq. (5).

It has been shown that the semi-local functionals fail to construct accurate band-structures in the case of noble metals and lead to erroneous inter-band transition spectra. The over-flattening of the electronic bands (particularly the fully filled d -bands) due to missing non-local quantum many-

body effects within the semi-local functionals were corrected by the real-time G_0W_0 . Through this corrective measure, the valence bands are more steepen than the conduction bands as the self-energy exchange term mostly acts on the occupied bands. This leads to an overall shift on the inter-band transitions to the higher energies. Comparison between the absorption spectra within the KS+RPA, QP+RPA and the experimental absorption spectra of the 3H-HCP polytypes showed that the KS+RPA erroneously predicts the absorption peaks at the lower energies, while the QP+RPA shifted them closer to the experimental values due to steepening of the electronic-band dispersions by the G_0W_0 correction. As a result, the first-principles Drude tails nicely match the experimental curves of the 3H-HCP phases at around 100 – 200 K as shown in Figs. 5 - 7.

We have investigated LSRPs in the perfectly spherical NPs embedded onto the silica-like hosting matrices. The increasing temperature shortens the LSPR lifetimes and generally shifts the LSPR peaks to the lower energies. This is due to the significant temperature-dependence of η_p which mostly determine the LSPR inverse lifetime (η) in Eq. (9) and lower the peak position through Eq. (8). The finite-size effect ($\alpha \neq 0$ in Eq. (9)) further shortens the LSPR lifetime. As the finite-size contribution in Eq. (9) is inversely proportional to the effective path length, the increasing NP radius (R) increases the LSPR lifetimes. The increasing dielectric permittivity of the hosting matrix (\mathcal{E}_m) shifts the LSPR peaks to the lower energies. These mechanisms alongside the available polytype give a wide-range control over the tuning the surface-plasmons for a designated application. At the technologically relevant 830 nm wavelength and for an operational temperature of 400 K, the 2H-HCP and 4H-HCP spherical NPs with 20 nm radius generate substantially stronger LSPR compared to their 3H-HCP counterparts (see Table S4) The Cu-4H-HCP NP is an exception with quite similar LSPR with the Cu-3H-HCP NP. Despite the more intense LSPR at 830 nm, the LSPR lifetimes in the 2H-HCP and 4H-HCP NPs are shorter compared to their 3H-HCP counterparts. However, their LSPR are still reasonably long-living, i.e., in the order of 1 fs.

The 2H-HCP and 4H-HCP phases of Ag is mechanically stronger compared to the Ag-3H-HCP, whilst the 3H-HCP phases of Au and Ag are superior compared to their other phases. Without any exception, the 2H-HCP and 4H-HCP phases exhibited lower thermal conductivity compared to their 3H-HCP counterpart.

The exotic HCP-based phases of noble metals can be promising alternatives for a wider-range plasmonic applications in terms of operational wavelengths, temperatures, ambient stress and thermal conditions. This work provides a reference work for these materials and a systematic workflow to study similar structures using the expedient first-principle methods.

V. ACKNOWLEDGEMENTS

We acknowledge the support from the rom the Natural Sciences and Engineering Research Council of Canada (NSERC) through the Discovery Grant under Award Application Number RGPIN-2016-06114, and the New Frontiers in Research Fund (NFRFE-2019-01095). This research was supported in part through computational resources and services provided by Advanced Research Computing at the University of British Columbia.

-
- [1] C. Black, S. Gates, C. Murray, and S. Sun, [Magnetic storage medium formed of nanoparticles](#) (2000).
 - [2] M. Mansuripur, A. R. Zakharian, A. Lesuffleur, S.-H. Oh, R. J. Jones, N. C. Lindquist, H. Im, A. Kobayakov, and J. V. Moloney, Plasmonic nano-structures for optical data storage, [Opt. Express](#) **17**, 14001 (2009).
 - [3] I. Sato, T. Oike, and N. Hanashima, Heat assisted magnetic recording head and heat assisted magnetic recording apparatus for heating a recording region in a magnetic recording medium during magnetic recording (2009), uS Patent 7,538,978.
 - [4] J. Zou, K. Gao, W. Challener, M. Ostrowski, V. Inturi, T. Zhao, and M. Kautzky, [Recording head for heat assisted magnetic recording with diffusion barrier surrounding a near field transducer](#) (2014).
 - [5] M. Alagiri, P. Rameshkumar, and A. Pandikumar, Gold nanorod-based electrochemical sensing of small biomolecules: A review, [Microchimica Acta](#) **184**, 3069 (2017).
 - [6] S. Bengali and M. Giri, [Gold sensor](#) (2018), US Patent App. 15/749,036.
 - [7] M. Rodrigues, D. Costa, R. Domingues, M. Apreutesei, P. Pedrosa, N. Martin, V. Correlo, R. Reis, E. Alves, N. Barradas, P. Sampaio, J. Borges, and F. Vaz, Optimization of nanocomposite Au/TiO₂ thin films towards lspr optical-sensing, [Applied Surface Science](#) **438**, 74 (2018), 10th International Conference on Materials Science & Engineering.
 - [8] P. K. Jain, X. Huang, I. H. El-Sayed, and M. A. El-Sayed, Noble metals on the nanoscale: Optical and photothermal properties and some applications in imaging, sensing, biology, and medicine, [Accounts of Chemical Research](#) **41**, 1578 (2008).
 - [9] K.-S. Lee and M. A. El-Sayed, Gold and silver nanoparticles in sensing and imaging: sensitivity of plasmon response to size, shape, and metal composition, [The Journal of Physical Chemistry B](#) **110**, 19220 (2006), <http://dx.doi.org/10.1021/jp062536y>.
 - [10] S. Medici, M. Peana, V. M. Nurchi, J. I. Lachowicz, G. Crisponi, and M. A. Zoroddu, Noble metals in medicine: Latest advances, [Coordination Chemistry Reviews](#) **284**, 329 (2015).
 - [11] P. K. Jain, I. H. El-Sayed, and M. A. El-Sayed, Au nanoparticles target cancer, [Nano Today](#) **2**, 18 (2007).

- [12] X. Zhang, Gold nanoparticles: Recent advances in the biomedical applications, *Cell Biochemistry and Biophysics* **72**, 771 (2015).
- [13] S. Tran, P.-J. DeGiovanni, B. Piel, and P. Rai, Cancer nanomedicine: a review of recent success in drug delivery, *Clinical and Translational Medicine* **6**, 44 (2017).
- [14] W. M. Abbott, C. P. Murray, C. Zhong, C. Smith, C. McGuinness, E. Rezvani, C. Downing, D. Daly, A. K. Petford-Long, F. Bello, D. McCloskey, and J. F. Donegan, Less is more: Improved thermal stability and plasmonic response in Au films via the use of subnanometer Ti adhesion layers, *ACS Applied Materials & Interfaces* **11**, 7607 (2019).
- [15] M. G. Blaber, M. D. Arnold, and M. J. Ford, A review of the optical properties of alloys and inter-metallics for plasmonics, *Journal of Physics: Condensed Matter* **22**, 143201 (2010).
- [16] B. Dastmalchi, P. Tassin, T. Koschny, and C. M. Soukoulis, A new perspective on plasmonics: Confinement and propagation length of surface plasmons for different materials and geometries, *Advanced Optical Materials* **4**, 177 (2016).
- [17] D. Beaglehole and E. Erlbach, Electronic structure of noble-metal-noble-metal alloys, *Phys. Rev. B* **6**, 1209 (1972).
- [18] Y. Nishijima, Y. Hashimoto, G. Seniutinas, L. Rosa, and S. Juodkazis, Engineering gold alloys for plasmonics, *Applied Physics A* **117**, 641 (2014).
- [19] C. Gong and M. S. Leite, Noble metal alloys for plasmonics, *ACS Photonics* **3**, 507 (2016).
- [20] Y. Hashimoto, G. Seniutinas, A. Balčytis, S. Juodkazis, and Y. Nishijima, Au-Ag-Cu nano-alloys: tailoring of permittivity, *Scientific reports* **6** (2016).
- [29] O. K. Orhan and D. D. O'Regan, Plasmonic performance of $\text{Au}_x\text{Ag}_y\text{Cu}_{1-x-y}$ alloys from many-body perturbation theory, *Journal of Physics: Condensed Matter* **31**, 315901 (2019).
- [22] F. Bello, O. K. Orhan, N. Abadía, D. D. O'Regan, and J. F. Donegan, Material characterization and thermal performance of au alloys in a thin-film plasmonic waveguide, in *Conference on Lasers and Electro-Optics* (Optical Society of America, 2019) p. JTu2A.110.
- [23] X. Huang, S. Li, Y. Huang, S. Wu, X. Zhou, S. Li, C. L. Gan, F. Boey, C. A. Mirkin, and H. Zhang, Synthesis of hexagonal close-packed gold nanostructures, *Nature Communications* **2**, 292 (2011).
- [24] K. Bian, H. Schunk, D. Ye, A. Hwang, T. S. Luk, R. Li, Z. Wang, and H. Fan, Formation of self-assembled gold nanoparticle supercrystals with facet-dependent surface plasmonic coupling, *Nature Communications* **9**, 2365 (2018).
- [25] Z. Fan, M. Bosman, Z. Huang, Y. Chen, C. Ling, L. Wu, Y. A. Akimov, R. Laskowski, B. Chen, P. Ercius, J. Zhang, X. Qi, M. H. Goh, Y. Ge, Z. Zhang, W. Niu, J. Wang, H. Zheng, and H. Zhang, Heterophase fcc-2h-fcc gold nanorods, *Nature Communications* **11**, 3293 (2020).
- [26] Z. Fan, M. Bosman, X. Huang, D. Huang, Y. Yu, K. P. Ong, Y. A. Akimov, L. Wu, B. Li, J. Wu, Y. Huang, Q. Liu, C. Eng Png, C. Lip Gan, P. Yang, and H. Zhang, Stabilization of 4h hexagonal phase in gold nanoribbons, *Nature Communications* **6**, 7684 (2015).

- [27] S. Han, G.-J. Xia, C. Cai, Q. Wang, Y.-G. Wang, M. Gu, and J. Li, Gas-assisted transformation of gold from fcc to the metastable 4h phase, *Nature Communications* **11**, 552 (2020).
- [28] H. Benaissa and M. Ferhat, Polytypism-induced stabilization of hexagonal 2h, 4h and 6h phases of gold, *Superlattices and Microstructures* **109**, 170 (2017).
- [29] I. Chakraborty, D. Carvalho, S. N. Shirodkar, S. Lahiri, S. Bhattacharyya, R. Banerjee, U. Waghmare, and P. Ayyub, Novel hexagonal polytypes of silver: growth, characterization and first-principles calculations, *Journal of Physics: Condensed Matter* **23**, 325401 (2011).
- [30] R. Thevamaran, O. Lawal, S. Yazdi, S.-J. Jeon, J.-H. Lee, and E. L. Thomas, Dynamic creation and evolution of gradient nanostructure in single-crystal metallic microcubes, *Science* **354**, 312 (2016).
- [31] R. Thevamaran, C. Griesbach, S. Yazdi, M. Ponga, H. Alimadadi, O. Lawal, S.-J. Jeon, and E. L. Thomas, Dynamic martensitic phase transformation in single-crystal silver microcubes, *Acta Materialia* **182**, 131 (2020).
- [32] D. F. Rojas, O. K. Orhan, and M. Ponga, Dynamic recrystallization of silver nanocubes during high-velocity impacts, *Acta Materialia* , 116892 (2021).
- [33] T. H. Fang, W. L. Li, N. R. Tao, and K. Lu, Revealing extraordinary intrinsic tensile plasticity in gradient nano-grained copper, *Science* **331**, 1587 (2011), <https://science.sciencemag.org/content/331/6024/1587.full.pdf>.
- [34] M. I. Novgorodova, A. I. Gorshkov, and A. V. Mokhov, Native silver and its new structural modifications, *International Geology Review* **23**, 485 (1981), <https://doi.org/10.1080/00206818109455083>.
- [35] E. Wetli, M. Hochstrasser, and M. Erbudak, Epitaxial growth of ag in the hexagonal structure, *Surface Science* **377-379**, 876 (1997), european Conference on Surface Science.
- [36] F. S. Ameer, S. Varahagiri, D. W. Benza, D. R. Willett, Y. Wen, F. Wang, G. Chumanov, and J. N. Anker, Tuning localized surface plasmon resonance wavelengths of silver nanoparticles by mechanical deformation, *The Journal of Physical Chemistry C* **120**, 20886 (2016).
- [37] Z. Fan, Y. Chen, Y. Zhu, J. Wang, B. Li, Y. Zong, Y. Han, and H. Zhang, Epitaxial growth of unusual 4h hexagonal ir, rh, os, ru and cu nanostructures on 4h au nanoribbons, *Chem. Sci.* **8**, 795 (2017).
- [38] P. Hohenberg and W. Kohn, Inhomogeneous electron gas, *Phys. Rev.* **136**, B864 (1964).
- [39] W. Kohn and L. J. Sham, Self-consistent equations including exchange and correlation effects, *Phys. Rev.* **140**, A1133 (1965).
- [40] X. Gonze, First-principles responses of solids to atomic displacements and homogeneous electric fields: Implementation of a conjugate-gradient algorithm, *Phys. Rev. B* **55**, 10337 (1997).
- [41] X. Gonze and C. Lee, Dynamical matrices, born effective charges, dielectric permittivity tensors, and interatomic force constants from density-functional perturbation theory, *Phys. Rev. B* **55**, 10355 (1997).
- [14] D. Bohm and D. Pines, A collective description of electron interactions. I. magnetic interactions, *Phys. Rev.* **82**, 625 (1951).
- [15] D. Pines and D. Bohm, A collective description of electron interactions: II. collective vs individual particle aspects of the interactions, *Phys. Rev.* **85**, 338 (1952).

- [16] D. Bohm and D. Pines, A collective description of electron interactions: III. coulomb interactions in a degenerate electron gas, *Phys. Rev.* **92**, 609 (1953).
- [17] A. D. McLachlan and M. A. Ball, Time-dependent Hartree-Fock theory for molecules, *Rev. Mod. Phys.* **36**, 844 (1964).
- [46] F. Aryasetiawan and O. Gunnarsson, The GW method, *Reports on Progress in Physics* **61**, 237 (1998).
- [31] T. Rangel, M. Del Ben, D. Varsano, G. Antonius, F. Bruneval, F. H. da Jornada, M. J. van Setten, O. K. Orhan, D. D. O'Regan, A. Canning, A. Ferretti, A. Marini, G.-M. Rignanese, J. Deslippe, S. G. Louie, and J. B. Neaton, Reproducibility in G_0W_0 calculations for solids, *Computer Physics Communications* **255**, 107242 (2020).
- [48] L. Landau, The theory of a fermi liquid, *Soviet Physics JETP-USSR* **3**, 920 (1957).
- [49] L. Landau, Oscillations in a fermi liquid, *Soviet Physics JETP-USSR* **5**, 101 (1957).
- [50] L. Landau, On the theory of the fermi liquid, *Sov. Phys. JETP* **8**, 70 (1959).
- [51] P. Drude, Zur elektronentheorie der metalle, *Annalen der Physik* **306**, 566 (1900).
- [52] P. Drude, Zur elektronentheorie der metalle; ii. teil. galvanomagnetische und thermomagnetische effecte, *Annalen der Physik* **308**, 369 (1900).
- [53] H. A. Lorentz, *The Theory of Electrons and Its Applications to the Phenomena of Light and Radiant Heat: A Course of Lectures Delivered in Columbia University, New York, in March and April, 1906*, Vol. 29 (Columbia University Press, 1909).
- [54] M. Fox, *Optical properties of solids*, Vol. 3 (Oxford university press, 2010).
- [55] N. Abadía, F. Bello, C. Zhong, P. Flanigan, D. M. McCloskey, C. Wolf, A. Krichinsky, D. Wolf, F. Zong, A. Samani, D. V. Plant, and J. F. Donegan, Optical and thermal analysis of the light-heat conversion process employing an antenna-based hybrid plasmonic waveguide for hamr, *Opt. Express* **26**, 1752 (2018).
- [56] X. X. Anurup Datta, Comparative study of optical near-field transducers for heat-assisted magnetic recording, *Optical Engineering* **56**, 1 (2017).
- [57] H. Yang, J. Li, and G. Xiao, Decay and propagation properties of symmetric surface plasmon polariton mode in metal-insulator-metal waveguide, *Optics Communications* **395**, 159 (2017), nano-Optoelectronics: Advanced Optoelectronic Devices Based on Nanostructures and Nanomaterials.
- [58] D. C. Langreth and J. P. Perdew, Theory of nonuniform electronic systems. i. analysis of the gradient approximation and a generalization that works, *Phys. Rev. B* **21**, 5469 (1980).
- [59] J. P. Perdew, Density-functional approximation for the correlation energy of the inhomogeneous electron gas, *Phys. Rev. B* **33**, 8822 (1986).
- [60] J. P. Perdew, J. A. Chevary, S. H. Vosko, K. A. Jackson, M. R. Pederson, D. J. Singh, and C. Fiolhais, Atoms, molecules, solids, and surfaces: Applications of the generalized gradient approximation for exchange and correlation, *Phys. Rev. B* **46**, 6671 (1992).
- [61] M. Born and K. Huang, *Dynamical theory of crystal lattices*, Oxford classic texts in the physical sciences (Clarendon Press, Oxford, 1954).

- [62] H. Demarest, R. Ota, and O. Anderson, Prediction of high pressure phase transitions by elastic constant data, in *High-Pressure Research*, edited by M. H. Manghnani and S.-I. Akimoto (Academic Press, 1977) pp. 281–301.
- [63] S. P. Rudin, Generalization of soft phonon modes, *Phys. Rev. B* **97**, 134114 (2018).
- [64] T. Rangel, D. Kecik, P. E. Trevisanutto, G.-M. Rignanese, H. Van Swygenhoven, and V. Olevano, Band structure of gold from many-body perturbation theory, *Phys. Rev. B* **86**, 125125 (2012).
- [65] D. Pines, *Elementary excitations in solids* (Perseus, 1966).
- [66] W. G. Aulbur, L. Jönsson, and J. W. Wilkins, Quasiparticle calculations in solids, *Solid State Physics* **54**, 1 (2000).
- [67] A. Marini, *Optical and electronic properties of Copper and Silver: from Density Functional Theory to Many Body Effects*, Ph.D. thesis, PhD Dissertation, University of Rome-Tor Vergata (2001).
- [68] J. A. McKay and J. A. Rayne, Temperature dependence of the infrared absorptivity of the noble metals, *Phys. Rev. B* **13**, 673 (1976).
- [69] V. Gasparov and R. Huguenin, Electron-phonon, electron-electron and electron-surface scattering in metals from ballistic effects, *Advances in Physics* **42**, 393 (1993).
- [70] S. Ogawa, H. Nagano, and H. Petek, Hot-electron dynamics at Cu(100), Cu(110), and Cu(111) surfaces: comparison of experiment with fermi-liquid theory, *Phys. Rev. B* **55**, 10869 (1997).
- [71] S. Dal Forno, L. Ranno, and J. Lischner, Material, size, and environment dependence of plasmon-induced hot carriers in metallic nanoparticles, *The Journal of Physical Chemistry C* **122**, 8517 (2018).
- [72] I. Y. Sklyadneva, E. V. Chulkov, W.-D. Schöne, V. M. Silkin, R. Keyling, and P. M. Echenique, Role of electron-phonon interactions versus electron-electron interactions in the broadening mechanism of the electron and hole linewidths in bulk be, *Phys. Rev. B* **71**, 174302 (2005).
- [73] P. Hofmann, I. Y. Sklyadneva, E. D. L. Rienks, and E. V. Chulkov, Electron-phonon coupling at surfaces and interfaces, *New Journal of Physics* **11**, 125005 (2009).
- [74] S. Poncé, E. Margine, C. Verdi, and F. Giustino, Epw: Electron-phonon coupling, transport and superconducting properties using maximally localized wannier functions, *Computer Physics Communications* **209**, 116 (2016).
- [75] M. H. Cohen, Optical constants, heat capacity and the fermi surface, *Philosophical Magazine* **3**, 762 (1958).
- [76] G. Grimvall, The electron-phonon interaction in normal metals, *Physica Scripta* **14**, 63 (1976).
- [77] U. Kreibig and M. Vollmer, Theoretical considerations, in *Optical Properties of Metal Clusters* (Springer Berlin Heidelberg, Berlin, Heidelberg, 1995) pp. 13–201.
- [78] O. Yeshchenko, I. Bondarchuk, V. Gurin, I. Dmitruk, and A. Kotko, Temperature dependence of the surface plasmon resonance in gold nanoparticles, *Surface Science* **608**, 275 (2013).
- [79] E. A. Coronado and G. C. Schatz, Surface plasmon broadening for arbitrary shape nanoparticles: A geometrical probability approach, *The Journal of Chemical Physics* **119**, 3926 (2003).

- [80] C. Novo, D. Gomez, J. Perez-Juste, Z. Zhang, H. Petrova, M. Reismann, P. Mulvaney, and G. V. Hartland, Contributions from radiation damping and surface scattering to the linewidth of the longitudinal plasmon band of gold nanorods: a single particle study, *Phys. Chem. Chem. Phys.* **8**, 3540 (2006).
- [81] A. Argon, *Strengthening mechanisms in crystal plasticity*, Vol. 4 (Oxford University Press on Demand, 2008).
- [82] X. Wu, P. Jiang, L. Chen, F. Yuan, and Y. T. Zhu, Extraordinary strain hardening by gradient structure, *Proceedings of the National Academy of Sciences* **111**, 7197 (2014), <https://www.pnas.org/content/111/20/7197.full.pdf>.
- [83] X. Zhou, X. Li, and K. Lu, Strain hardening in gradient nano-grained cu at 77k, *Scripta Materialia* **153**, 6 (2018).
- [84] S. Pugh, Relations between the elastic moduli and the plastic properties of polycrystalline pure metals, *The London, Edinburgh, and Dublin Philosophical Magazine and Journal of Science* **45**, 823 (1954).
- [85] S. Boucetta, Theoretical study of elastic, mechanical and thermodynamic properties of mgrh inter-metallic compound, *Journal of Magnesium and Alloys* **2**, 59 (2014).
- [86] I. Brooks, P. Lin, G. Palumbo, G. Hibbard, and U. Erb, Analysis of hardness–tensile strength relationships for electroformed nanocrystalline materials, *Materials Science and Engineering: A* **491**, 412 (2008).
- [87] D. M. Teter, Computational alchemy: The search for new superhard materials, *MRS Bulletin* **23**, 22–27 (1998).
- [88] D. T. Morelli and G. A. Slack, High lattice thermal conductivity solids, in *High Thermal Conductivity Materials*, edited by S. L. Shindé and J. S. Goela (Springer New York, New York, NY, 2006) pp. 37–68.
- [89] Y. M. Jin, Y. U. Wang, and Y. Ren, Theory and experimental evidence of phonon domains and their roles in pre-martensitic phenomena, *npj Computational Materials* **1**, 15002 (2015).
- [90] S. Babar and J. H. Weaver, Optical constants of cu, ag, and au revisited, *Appl. Opt.* **54**, 477 (2015).
- [91] E. D. Palik, *Handbook of optical constants of solids*, Vol. 3 (Academic press, 1998).
- [92] M. Rocca, Low-energy eels investigation of surface electronic excitations on metals, *Surface Science Reports* **22**, 1 (1995).
- [93] J. Robertson, High dielectric constant oxides, *The European Physical Journal - Applied Physics* **28**, 265–291 (2004).
- [94] Y. S. Touloukian, R. W. Powell, C. Y. Ho, and P. G. Klemens, *Thermophysical properties of matter - the TPRC data series. Volume 1. Thermal conductivity - metallic elements and alloys. (Reannouncement). Data book*, Tech. Rep. (United States, 1970).
- [95] R. T. Beach and R. W. Christy, Electron-electron scattering in the intraband optical conductivity of cu, ag, and au, *Phys. Rev. B* **16**, 5277 (1977).

Supporting Information

”Surface-plasmon properties of noble metals with exotic phases”

I. APPROXIMATE GIBBS FREE ENERGY

For a non-magnetic elemental and pristine solid, the Gibbs free energy (GFE) is given by

$$G(V, T) = H(V) + F_{\text{el}}(V, T) + F_{\text{vib}}(V, T), \quad (\text{S1})$$

where $H(V)$ is the formation enthalpy, $F_{\text{el}}(V, T)$ and $F_{\text{vib}}(V, T)$ are the electronic and vibrational Helmholtz free energies, respectively. At the equilibrium volumes, the formation enthalpy can be simply approximated by the ground-state energy within the approximate KS-DFT such as $H(V) = E_0$.

The electronic Helmholtz free energy for metallic systems is approximated by [S1–S3]

$$F_{\text{el}} = \left(\int dE N(E, V) f E - \int^{E_F} dE N(E, V) E \right) - T \left(-k_B \int dE N(E, V) [f \ln(f) + (1 - f) \ln(1 - f)] \right), \quad (\text{S2})$$

where k_B is the Boltzmann constant, $N(E, V)$ is the electron density of states (DOS), $f = f(E, E_F, T)$ is the Fermi-Dirac distribution function around the Fermi level with the Fermi energy, E_F . The first term is the energy of free electrons, whilst the second term is due to electronic excitation above the Debye temperature by ignoring magnetic and electron-phonon (e-ph) couplings. The vibrational Helmholtz free energy for lattice ions within the quasi-harmonic approximation using the phonon dispersion is given by [S4, S5]

$$F_{\text{vib}}(T, V) = k_B T \int_0^\infty d\omega \ln \left[2 \sinh \left(\frac{\hbar \omega}{2 k_B T} \right) \right] g(\omega), \quad (\text{S3})$$

where $g(\omega)$ is the phonon DOS. $k_B T$ is the usual thermodynamic factor, where k_B is the Boltzmann’s constant and T the absolute temperature, and ω is the vibration frequency of the phonon modes.

II. ELASTIC PROPERTIES

The necessary and sufficient conditions for hexagonal symmetry is given by [S6]

$$c_{11} > |c_{12}|, \quad c_{33} (c_{11} + c_{12}) > 2c_{13}^2, \quad \text{and} \quad c_{44} > 0, \quad (\text{S4})$$

where the components c_{ij} , $i = j = 1, 2, 3$ of the second-order elastic tensor. The second-order elastic tensor is commonly calculated by performing a series of ground-state calculations on the infinitesimal-strained structures. The elastic constants are then calculated from the changes of the energy density with respect to the strain components. The bulk and shear modulus can be derived using the second-order elastic tensor within the the Voigt-Reuss-Hill (VRH) averaging [S7–S9]. Young's modulus, the approximate sound velocities, the Poisson ratio and the approximate Debye temperature through their relation to the bulk and shear modulus. The Voigt-Reuss-Hill averaged bulk and shear modulus, symbolically B and S , respectively, are given by

$$B_{\text{VHR}} = \frac{B_{\text{V}} + B_{\text{R}}}{2}, \quad \text{and} \quad S_{\text{VHR}} = \frac{S_{\text{V}} + S_{\text{R}}}{2}, \quad (\text{S5})$$

for which the Voigt and Reuss averaging provide an upper-bound and a lower-bound, respectively. The Voigt- and Reuss-averaged bulk and shear modulus for hexagonal systems are related to the elements of the second-order elastic tensor, symbolically \mathbb{C} , by [S10]

$$\begin{aligned} B_{\text{V}} &= \frac{2(c_{11} + c_{12} + 0.5c_{33} + 2c_{13})}{9}, \quad \text{and} \quad B_{\text{R}} = \frac{1}{3\alpha + 6\beta}; \\ S_{\text{V}} &= \frac{7c_{11} - 5c_{12} + 12c_{44} + 2c_{33} - 4c_{13}}{30}, \quad \text{and} \quad S_{\text{R}} = \frac{5}{4\alpha - 4\beta + 3\lambda}, \end{aligned} \quad (\text{S6})$$

where $3\alpha = s_{11} + s_{11} + s_{33}$, $3\beta = s_{23} + s_{31} + s_{12}$, and $3\lambda = s_{44} + s_{55} + s_{66}$. s_{ij} are elements of the elastic compliance tensor given by $\mathbb{S} = \mathbb{C}^{-1}$. Using these two modulus, Young's modulus (Y) and the Poisson ratio (ν_{P}) are

$$Y = \frac{9BS}{3B + S}, \quad \text{and} \quad \nu_{\text{P}} = \frac{3B - 2S}{6B + 2S}. \quad (\text{S7})$$

Furthermore, the transverse (shear) and the longitudinal (compressional) wave velocities (v_{t} and v_{l} , respectively) are given by [S11]

$$v_{\text{l}} = \left[\left(KB \frac{4}{3} S \right) \frac{1}{\rho} \right]^{1/2}, \quad \text{and} \quad v_{\text{t}} = \left[\frac{S}{\rho} \right]^{1/2}, \quad (\text{S8})$$

where ρ is the density of solid. Finally, the Debye temperature can be approximated for equilibrium volume by [S11]

$$\Theta_D = \frac{h}{k_B} \left[\frac{3}{4\pi} \frac{N}{V_0} \right]^{1/3} v_s, \quad (\text{S9})$$

where N is the number of atoms in the unit cell and v_{av} is the average constant sound velocity. The average sound velocity, v_s , can be determined either by solving the Christoffel equation in each direction [S12], or approximately by the relation [S11]

$$v_s = \left(\frac{1}{3} \right)^{-1/3} \left[\frac{2}{v_t^3} + \frac{1}{v_l^3} \right]^{-1/3}. \quad (\text{S10})$$

Finally, the Grüneisen parameter is expediently given in terms of the Poisson's ratio (ν) by [S13]

$$\gamma = \frac{3(1 + \nu)}{2(2 - 3\nu)}. \quad (\text{S11})$$

III. RANDOM-PHASE APPROXIMATION

In the linear-response regime, the microscopic dielectric function is given by

$$\varepsilon_{\mathbf{G},\mathbf{G}'}^{-1}(\mathbf{q},\omega) = \delta_{\mathbf{G},\mathbf{G}'} + v_{\mathbf{G},\mathbf{G}'}(\mathbf{q})\chi_{\mathbf{G},\mathbf{G}'}(\mathbf{q},\omega), \quad (\text{S12})$$

where $v_{\mathbf{G},\mathbf{G}'}(\mathbf{q}) = 4\pi/(|\mathbf{q} + \mathbf{G}||\mathbf{q} + \mathbf{G}'|)$ is the bare Coulomb interaction and $\chi_{\mathbf{G},\mathbf{G}'}(\mathbf{q},\omega)$ is the interacting response function which is given within RPA by [S14–S17]

$$\chi_{\mathbf{G}\mathbf{G}'}(\mathbf{q},\omega) = \chi_{\mathbf{G}\mathbf{G}'}^0(\mathbf{q},\omega) (1 + v_{\mathbf{G},\mathbf{G}'}(\mathbf{q})\chi_{\mathbf{G}\mathbf{G}'}(\mathbf{q},\omega)), \quad (\text{S13})$$

which is a Dyson equation. $\chi_{\mathbf{G}\mathbf{G}'}^0$ is the non-interacting response function, given within Fermi's golden rule [S18] by

$$\chi_{\mathbf{G}\mathbf{G}'}^0(\mathbf{q},\omega) = 2 \sum_{c,v,\mathbf{k}} (f_{v,\mathbf{k}} - f_{c,\mathbf{k}-\mathbf{q}}) \frac{|\langle \psi_{c,\mathbf{k}-\mathbf{q}} | e^{i(\mathbf{q}+\mathbf{G})\cdot\mathbf{r}} | \psi_{v,\mathbf{k}} \rangle|^2}{\omega - \omega_{cv,\mathbf{k}\mathbf{q}} + i\Gamma}, \quad (\text{S14})$$

where $\psi_{i,\mathbf{k}}$ is the well-defined single-particle electronic states, $f_{i,\mathbf{k}}$ is its occupancy; the indices c and v are running over the conduction and valence bands, respectively. The inter-band part of the macroscopic dielectric function is obtained by summing over the first Brillouin zone at the vanishing momentum limit ($\mathbf{q} \rightarrow 0$) [S19].

IV. PERTURBATIVE QUASI-PARTICLE FORMALISM

The quasi-particle (QP) single-particle electronic wave-functions can be calculated by self-consistently solving the QP equation, which resembles to the KS equation with an additional self-energy terms and the QP re-normalization to the electronic mass. Assuming that the the KS and the QP eigenstates differ very little such as $\langle \psi_i | \psi_i^{\text{QP}} \rangle \approx 1$, a more practical approach is to perturbatively calculate the QP energies by

$$\epsilon_i^{\text{QP}} = \epsilon_i^{\text{KS}} + Z_i \langle \psi_i^{\text{KS}} | \hat{\Sigma}(\epsilon_i^{\text{KS}}) - \hat{v}_{\text{xc}}^{\text{KS}} | \psi_i^{\text{KS}} \rangle, \quad \text{and } Z_i = \left[1 - \frac{\partial \Sigma'(\omega)}{\partial \omega} \Big|_{\omega=\epsilon_i^{\text{KS}}} \right]^{-1}, \quad (\text{S15})$$

where Z_i is called the QP re-normalization factor and $\hat{v}_{\text{xc}}^{\text{KS}}$ is the KS exchange-correlation operator. Within the one-shot, non-self-consistent GW, or simply G_0W_0 , the self-energy operator can be calculated by the single iteration of Hedin's equations [S20, S21] when the vertex function is set to the Kronecker-Delta-function product. By doing so, it is simply $\Sigma = iG_0W_0$, where G_0 and W_0 are the non-interacting single-particle Green function and the screened Coulomb interactions, respectively.

V. COMPUTATIONAL DETAILS

The initial crystallographic information for the FCC Au, Ag, Cu were adopted from Ref. S22. They were used to construct 2H-HCP, 3H-HCP and 4H-HCP structures by following AB, ABC, ABAC stacking sequences, respectively. The in-house norm-conserving PBE pseudo-potentials were generated by the pseudo-potential generator OPIUM [S23]. The initial structures were optimized by using the variable-cell relaxation routine within the the Quantum ESPRESSO (QE) software [S24, S25] with a common high kinetic energy cutoff of 150 Ry and a choice of smearing parameter for the Marzari-Vanderbilt cold smearing [S26] of 0.1 eV. Structural optimization were performed on the $12 \times 12 \times 6$, $12 \times 12 \times 4$, and $12 \times 12 \times 3$ Monkhorst-Pack-equivalent [S27] Brillouin zone (k -point) samplings without any shift for the 2H-HCP, 3H-HCP and 4H-HCP structures, respectively. Convergence thresholds for the total energies, the total forces and the self-consistency were set to 10^{-7} Ry, 10^{-6} (Ry/ a_0^3) and 10^{-10} , respectively. For further simulations, a kinetic energy cutoff of 100 Ry was used as the common converged value by less than 1 meV per atom different in the total energies, whilst the Marzari-Vanderbilt cold smearing parameter was kept same. Other parameters were adjusted for each set of simulations.

In the first set of simulations the thermodynamic quantities, the elastic properties and the phonon dispersion were calculated using the *"thermo_pw"* package [S28] within the QE software. During these simulations, the Brillouin zone samplings, which were used in the geometry optimizations, were shifted by $1 \times 1 \times 1$. For the phonon dispersion simulations, the $2 \times 2 \times 6$, $2 \times 2 \times 4$ and $2 \times 2 \times 3$ Monkhorst-Pack-equivalent q -point samplings were used for the 2H-HCP, 3H-HCP and 4H-HCP structures, respectively.

The e-ph coupling calculations requires multiple simulations with carefully chosen Brillouin zone sampling for feasible computational cost. The first set of self-consistent-field (SCF) simulations were performed on a dense $24 \times 24 \times 24$ grid. These simulations were later used for fitting during the e-ph coupling matrix simulations. The second set of SCF simulations were performed in a less dense $12 \times 12 \times 12$ k -point grid. The e-ph coupling matrices were calculated on the previously used q -point samplings during the phonon dispersion simulations. The choice of the k -point and q -point samplings during these subsequent simulations, indeed, were dictated by the available methods within the QP software. The e-ph coupling matrices were evaluated for the five Gaussian broadening used in the double-delta integrals. These broadening parameters were chosen equivalently to a monotonically increasing temperature from 100 K to 500 K.

The third set of simulations were performed using the in-house code [S29] to calculate the Fermi velocities and the Drude plasmon energies. As these simulations requires the well-converged KS band-structures on a dense grid, the non-self-consistent-field (NSCF) simulations were performed on the $12 \times 12 \times 12$ k -point grids on top of the SCF simulations on the $24 \times 24 \times 24$ k -point grids. The Fermi levels and corresponding electronic DOS were chosen from the previous e-ph coupling simulations for each Gaussian broadening to match the electronic temperatures.

The last set of simulations were performed to obtain the approximate quasi-particle band-structures and the inter-band transitions using the Yambo software [S30]. Since the G_0W_0 simulations requires a large number of additional unoccupied KS states during calculating the self-energy correlations, the NSCF simulations were performed for a total of 100 bands for each spin-channel. For further details, we refer the reader to Ref. S31. The self-energies were calculated for the entire Brillouin zones, occupied bands and equal number of unoccupied bands. RPA simulations were performed on the approximate quasi-particle band-structures with a Lorentzian smearing parameter of full-width 0.2 eV.

A. Comparison of FCC and 3H-HCP crystal structures

	$\% \Delta a$	$\% \Delta c$	$\% \Delta d_{AB}$	$\% \Delta \alpha_{ABC}$
Au	-0.31	0.62	0.31	0.34
Ag	-0.11	0.46	0.27	0.21
Cu	-0.19	0.25	0.10	0.16

TABLE S1. Percentage relative differences of lattice parameters, bond lengths and angles between the fully relaxed 3H-HCP and FCC structures. All values are $< \%1$ indicating that the ideal FCC and 3H-HCP crystals are equivalent within the accuracy of the approximate KS-DFT.

VI. THERMAL AND MECHANICAL ASSESSMENTS

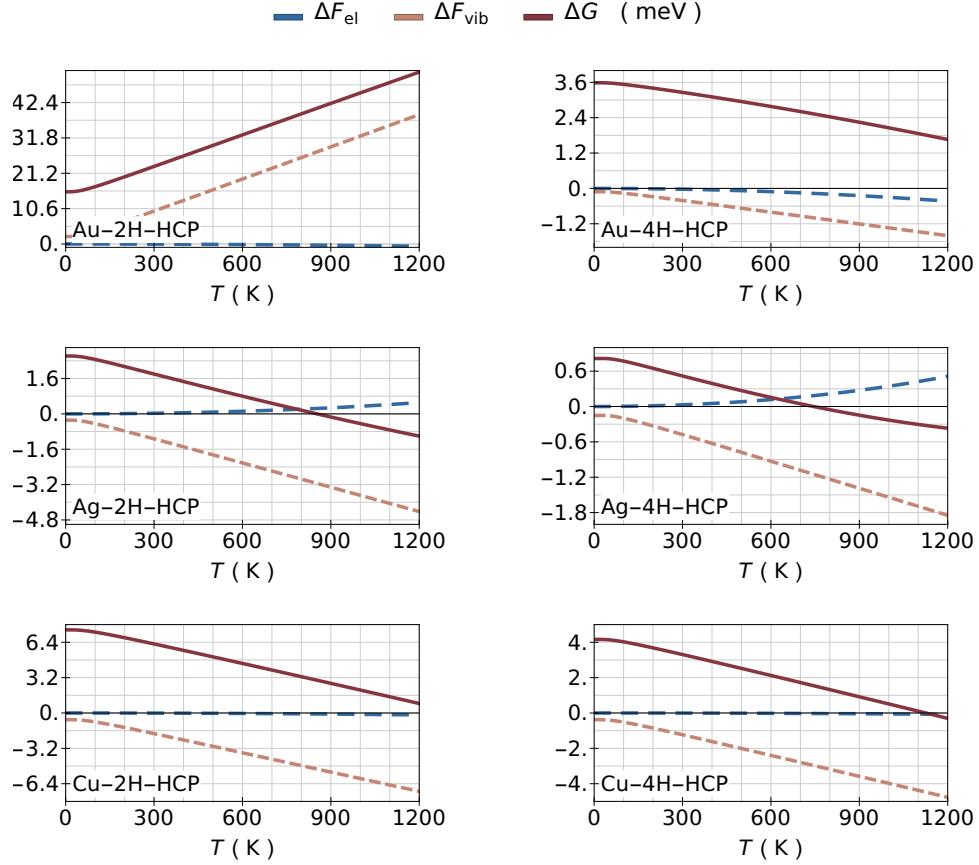


FIG. S1. Temperature dependence of the electronic (ΔF_{el}) and vibrational (ΔF_{vib}) Helmholtz free energy and the Gibbs free energy differences (ΔG) of 2H-HCP and 4H-HCP phases with respect to their 3H-HCP phases.

	c_{11}	c_{12}	c_{13}	c_{33}	c_{44}
Au-2H-HCP	201	127	109	184	16
Au-3H-HCP	205	118	117	209	28
Au-4H-HCP	202	119	116	213	23
Ag-2H-HCP	142	65	56	145	24
Ag-3H-HCP	144	67	56	152	22
Ag-4H-HCP	147	63	52	162	26
Cu-2H-HCP	215	91	92	238	51
Cu-3H-HCP	234	85	85	252	51
Cu-4H-HCP	213	102	91	229	49

TABLE S2. Five independent elastic constants (in GPa units) of the isolated Au, Ag and Cu polytypes.

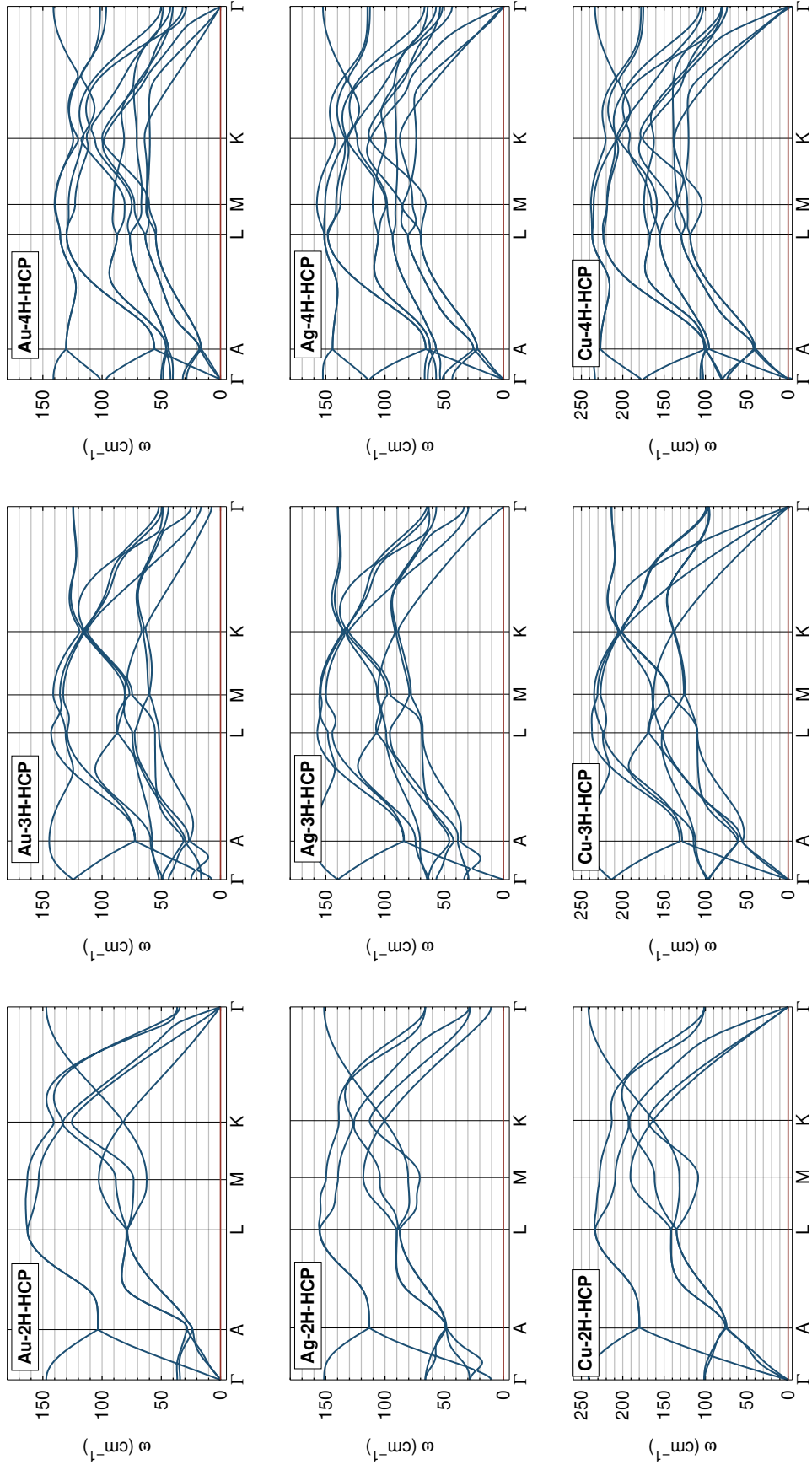


FIG. S2. Phonon dispersions of the isolated Au, Ag and Cu polytypes at their equilibrium volumes.

VII. TEMPERATURE-DEPENDENCE OF FERMI VELOCITIES, ELECTRON-PHONON MASS ENHANCEMENT PARAMETERS AND DRUDE PLASMON PARAMETERS

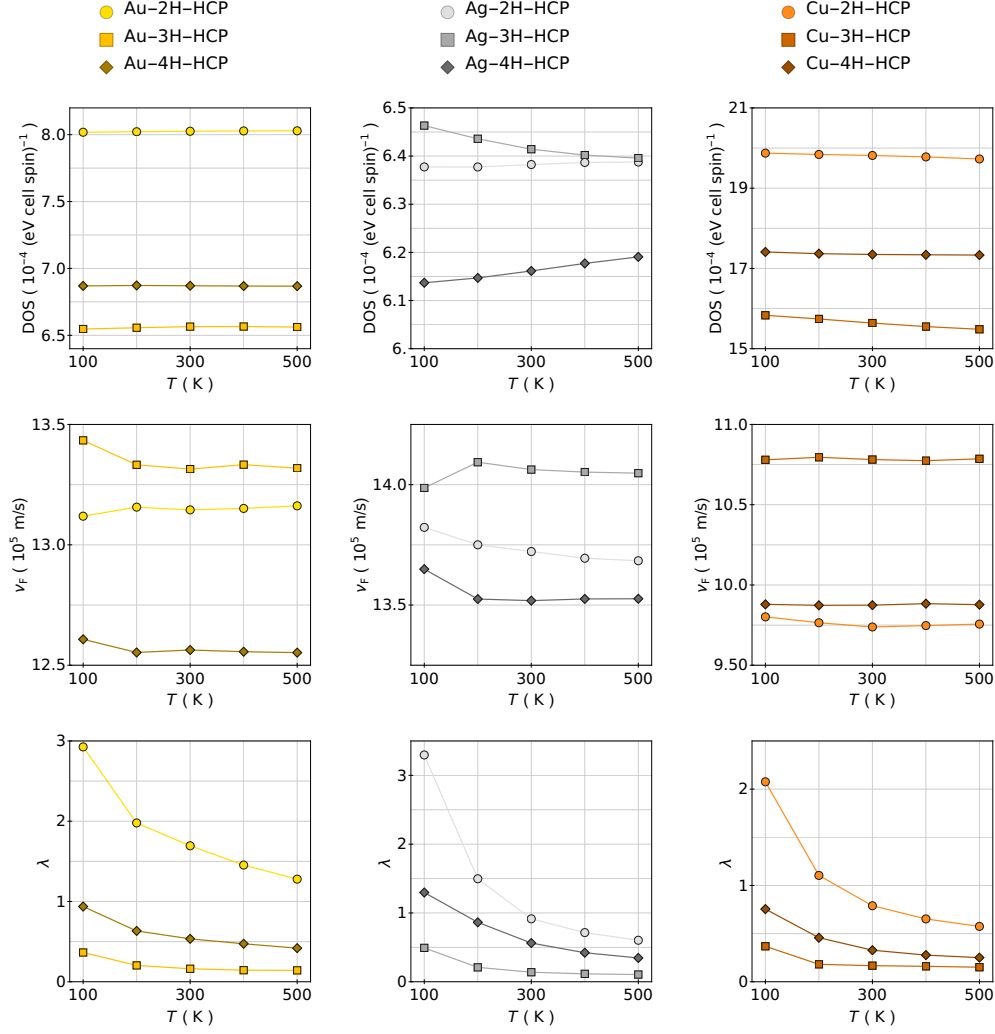


FIG. S3. Temperature dependence of the electronic density of states (DOS), the Fermi velocities (v_F) and the electron-phonon mass enhancement parameters (λ) of the isolated Au, Ag and Cu polytypes.

	100			200			300			400			500		
	ω_p	η_p	τ_p	ω_p	η_p	τ_p	ω_p	η_p	τ_p	ω_p	η_p	τ_p	ω_p	η_p	τ_p
Au-2H-HCP	3.875	0.192	21.519	3.887	0.384	10.757	3.884	0.577	7.169	3.887	0.769	5.375	3.890	0.962	4.299
Au-3H-HCP	8.304	0.018	224.470	8.247	0.037	111.768	8.241	0.056	74.205	8.253	0.075	55.424	8.242	0.094	44.156
Au-4H-HCP	6.046	0.061	68.104	6.021	0.122	34.012	6.025	0.183	22.648	6.021	0.244	16.966	6.019	0.305	13.556
Ag-2H-HCP	5.186	0.104	39.830	5.159	0.208	19.898	5.151	0.312	13.254	5.142	0.416	9.932	5.138	0.521	7.939
Ag-3H-HCP	8.864	0.016	261.521	8.913	0.032	130.040	8.878	0.048	86.214	8.863	0.064	64.304	8.856	0.081	51.162
Ag-4H-HCP	6.151	0.064	64.699	6.100	0.128	32.302	6.104	0.192	21.504	6.115	0.257	16.105	6.122	0.321	12.865
Cu-2H-HCP	5.757	0.090	46.204	5.730	0.179	23.098	5.711	0.269	15.396	5.711	0.358	11.545	5.709	0.448	9.235
Cu-3H-HCP	8.655	0.019	218.194	8.643	0.038	108.975	8.603	0.057	72.567	8.574	0.076	54.362	8.564	0.095	43.439
Cu-4H-HCP	7.312	0.037	111.196	7.298	0.074	55.571	7.295	0.112	37.029	7.300	0.149	27.758	7.294	0.186	22.196

TABLE S3. Drude plasmon energies (ω_p) in eV units, the inverse lifetimes (η_p) in eV units and lifetimes (τ_p) in fs units of the isolated Au, Ag and Cu polytypes at the available temperatures (in K units).

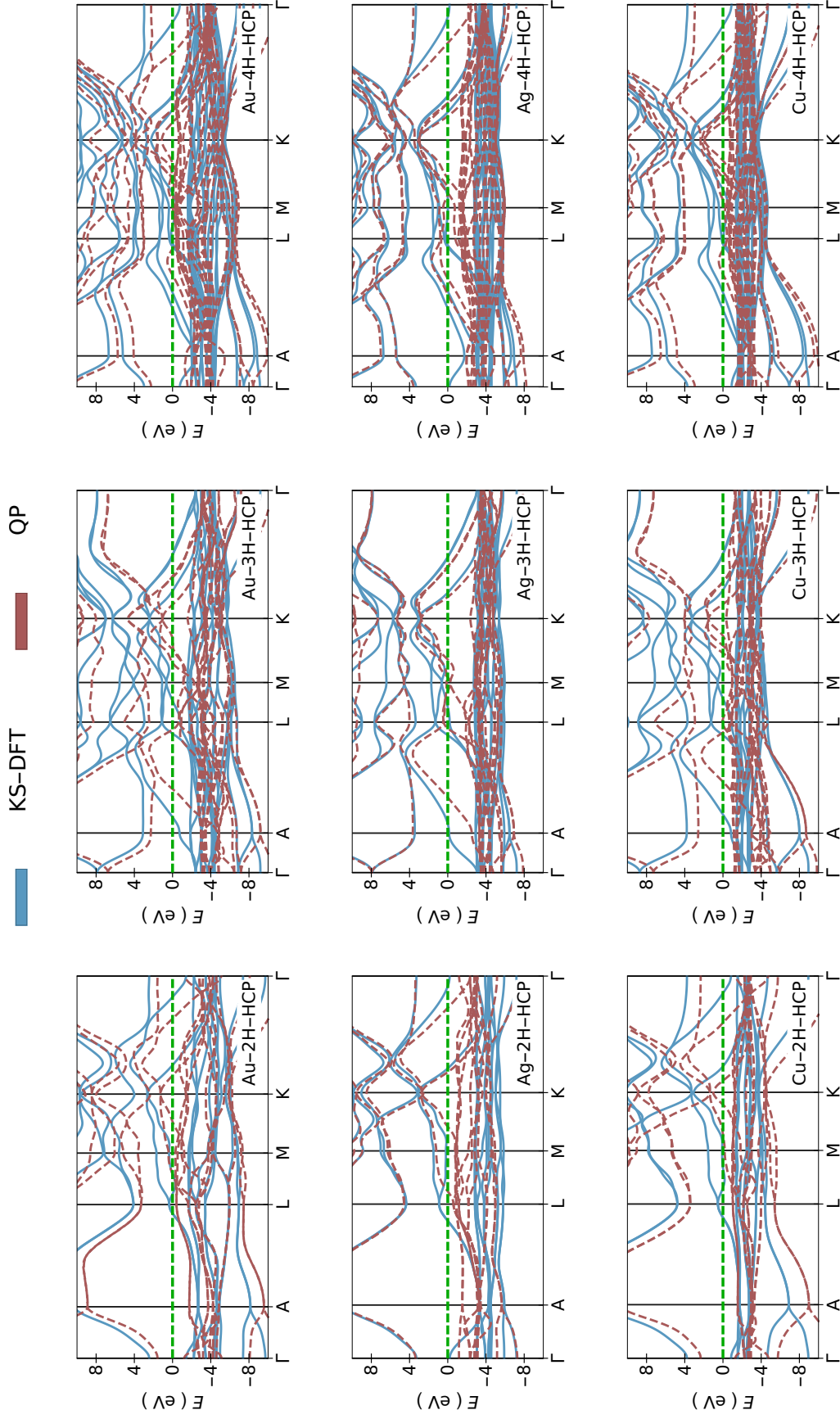


FIG. S4. Kohn-Sham band-structures (blue solid lines) and the approximate quasiparticle band-structure (red dashed lines). The Fermi levels are set to 0 eV.

VIII. TEMPERATURE-DEPENDENCE OF LOCALIZED SURFACE-PLASMONS

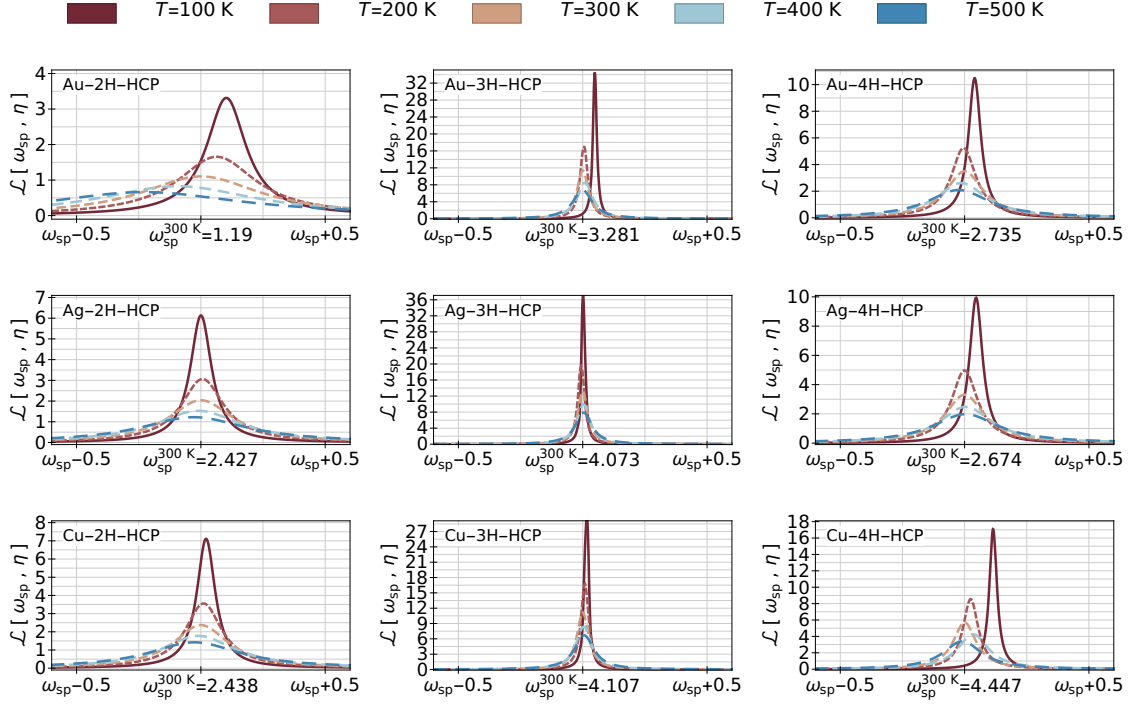


FIG. S5. Temperature dependence of the localized surface-plasmon resonance of noble-metal nanoparticles on a hosting matrix with the unit dielectric permittivity of $\mathcal{E}_m = 1.0$ when the geometry- and size-dependence of the inverse plasmon lifetime are ignored by setting $\alpha = 0.0 \rightarrow \eta = \eta_p$, shown using the Lorentzian line shape (\mathcal{L}).

IX. HOSTING-MATRIX AND SIZE-DEPENDENCE OF LOCALIZED SURFACE-PLASMON AT 400 K

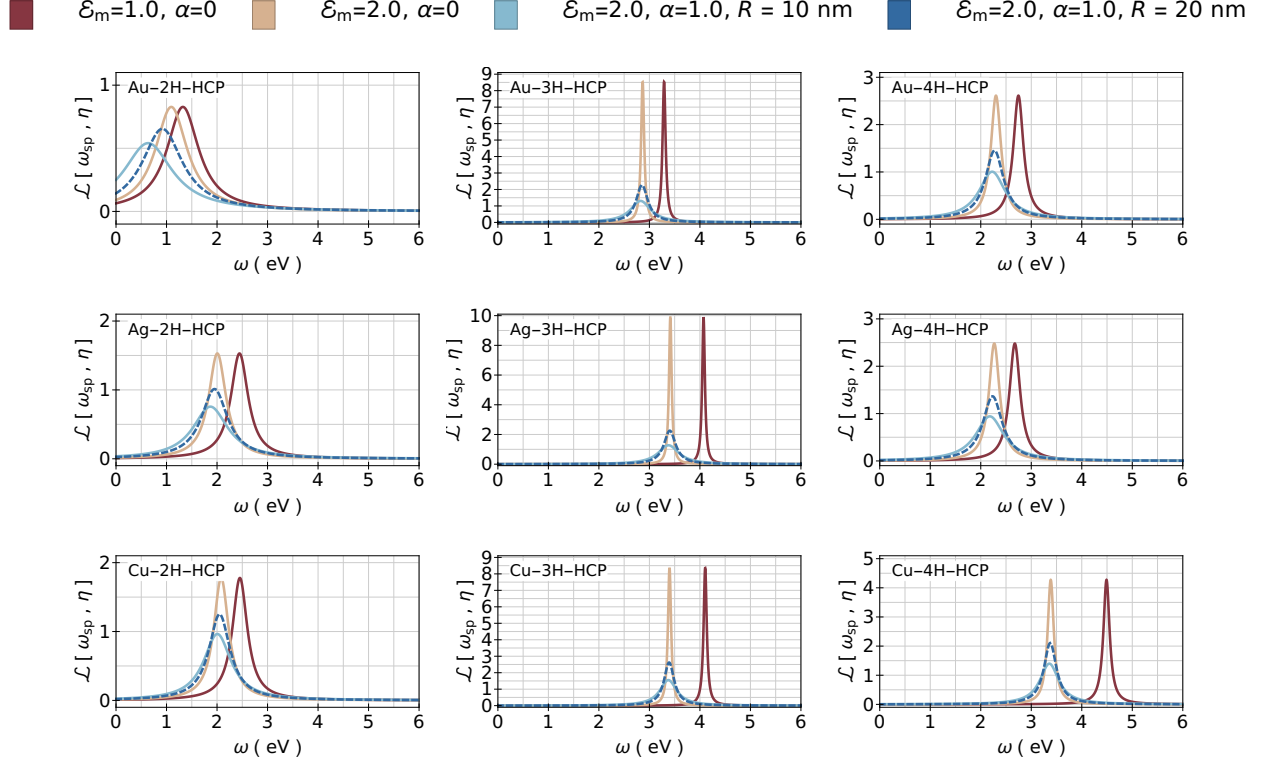


FIG. S6. Hosting-matrix dielectric matrix(ϵ_m), the theory-dependent constant (α) and the size-dependence, controlled by the nanoparticle radius (R), of the localized surface-plasmon resonance of noble-metal nanoparticles at $T = 400 \text{ K}$.

	λ	ω_p (eV)	η_p (eV)	ω_{sp} (eV)	η (eV)	τ (fs)	$\mathcal{L}[\omega_{sp}, \eta]$
Au-2H-HCP	1.454	3.887	0.769	0.895	0.973	4.249	0.260
Au-3H-HCP	0.144	8.253	0.075	2.794	0.281	14.697	0.026
Au-4H-HCP	0.473	6.021	0.244	2.001	0.438	9.431	0.229
Ag-2H-HCP	0.715	5.142	0.416	1.632	0.629	6.577	0.848
Ag-3H-HCP	0.115	8.863	0.064	3.002	0.282	14.653	0.020
Ag-4H-HCP	0.422	6.115	0.257	2.027	0.467	8.864	0.219
Cu-2H-HCP	0.652	5.711	0.358	1.875	0.509	8.119	0.386
Cu-3H-HCP	0.16	8.574	0.076	2.907	0.243	17.007	0.019
Cu-4H-HCP	0.277	7.300	0.149	2.465	0.302	13.682	0.050

TABLE S4. Localized surface-plasmon resonance in the spherical nanoparticles with radii of $R = 20$ nm and embedded on a hosting matrices with a dielectric permittivity, $\mathcal{E}_m = 4.0$ at the 830 nm (~ 1.494 eV) wavelength and at a temperature of $T = 400$ K.

X. MECHANICAL PROPERTIES

	B (GPa)	Y (GPa)	S (GPa)	ν_P	v_P (m/s)	v_B (m/s)	v_G (m/s)	v_D (m/s)	Θ_D (K)
Au-2H-HCP	141	67	24	0.42	3086	2791	1141	1257	143
Au-3H-HCP	147	95	34	0.39	3256	2845	1371	1537	175
Au-4H-HCP	147	74	26	0.41	3166	2843	1206	1346	153
Ag-2H-HCP	87	86	32	0.33	3666	2999	1826	2038	229
Ag-3H-HCP	89	77	29	0.35	3613	3022	1715	1889	213
Ag-4H-HCP	88	94	36	0.32	3740	3012	1921	2137	241
Cu-2H-HCP	135	151	57	0.31	5051	4036	2630	2938	375
Cu-3H-HCP	137	158	60	0.31	5111	4055	2695	2980	380
Cu-4H-HCP	136	141	53	0.33	4985	4043	2525	2822	360

TABLE S5. Elastic modulus, the Poisson ratios, sound velocities and the Debye temperatures of Au, Ag and Cu polytypes.

XI. TEMPERATURE DEPENDENCE OF THE TOTAL THERMAL CONDUCTIVITY

	100	200	300	400	500
Au-2H-HCP	9	9	9	10	11
Au-3H-HCP	263	323	342	351	349
Au-4H-HCP	42	52	57	61	66
Ag-2H-HCP	30	26	32	35	38
Ag-3H-HCP	280	409	452	465	469
Ag-4H-HCP	58	54	63	72	77
Cu-2H-HCP	86	69	71	73	75
Cu-3H-HCP	454	543	537	532	535
Cu-4H-HCP	163	184	206	217	222

TABLE S6. Temperature-dependent total thermal conductivity in the ($\text{W}\cdot\text{m}^{-1}\cdot\text{K}^{-1}$) units of the Au, Ag and Cu polytypes.

-
- [S1] Y. Wang, Z.-K. Liu, and L.-Q. Chen, Thermodynamic properties of Al, Ni, NiAl, and Ni₃Al from first-principles calculations, *Acta Materialia* **52**, 2665 (2004).
- [S2] L. Landau and E. Lifshitz, Statistical physics (Pergamon Press, Headington Hill Hall, Oxford, OX3 0BW England, 1980) Chap. 5, pp. 158–168, 3rd ed.
- [S3] F. Tian, A review of solid-solution models of high-entropy alloys based on ab initio calculations, *Frontiers in Materials* **4**, 36 (2017).
- [S4] A. van de Walle and G. Ceder, The effect of lattice vibrations on substitutional alloy thermodynamics, *Rev. Mod. Phys.* **74**, 11 (2002).
- [S5] S.-L. Shang, Y. Wang, D. Kim, and Z.-K. Liu, First-principles thermodynamics from phonon and Debye model: Application to Ni and Ni₃Al, *Computational Materials Science* **47**, 1040 (2010).
- [S6] F. Mouhat and F. m. Coudert, Necessary and sufficient elastic stability conditions in various crystal systems, *Phys. Rev. B* **90**, 224104 (2014).
- [S7] W. Voigt, Ueber die beziehung zwischen den beiden elasticitätsconstanten isotroper körper, *Annalen der Physik* **274**, 573 (1889), <https://onlinelibrary.wiley.com/doi/pdf/10.1002/andp.18892741206>.

- [S8] A. Reuss, Berechnung der fließgrenze von mischkristallen auf grund der plastizitätsbedingung für einkristalle ., *ZAMM - Journal of Applied Mathematics and Mechanics / Zeitschrift für Angewandte Mathematik und Mechanik* **9**, 49 (1929), <https://onlinelibrary.wiley.com/doi/pdf/10.1002/zamm.19290090104>.
- [S9] R. Hill, The elastic behaviour of a crystalline aggregate, *Proceedings of the Physical Society. Section A* **65**, 349 (1952).
- [S10] D. Tromans, Elastic anisotropy of hcp metal crystals and polycrystals, *Int. J. Res. Rev. Appl. Sci* **6**, 462 (2011).
- [S11] O. L. Anderson, A simplified method for calculating the Debye temperature from elastic constants, *Journal of Physics and Chemistry of Solids* **24**, 909 (1963).
- [S12] J. W. Jaeken and S. Cottenier, Solving the Christoffel equation: Phase and group velocities, *Computer Physics Communications* **207**, 445 (2016).
- [S13] Z.-Y. Jiao, T.-X. Wang, and S.-H. Ma, Phase stability, mechanical properties and lattice thermal conductivity of ceramic material $(\text{Nb}_{1-x}\text{Ti}_x)_4\text{AlC}_3$ solid solutions, *Journal of Alloys and Compounds* **687**, 47 (2016).
- [S14] D. Bohm and D. Pines, A collective description of electron interactions. I. magnetic interactions, *Phys. Rev.* **82**, 625 (1951).
- [S15] D. Pines and D. Bohm, A collective description of electron interactions: II. collective vs individual particle aspects of the interactions, *Phys. Rev.* **85**, 338 (1952).
- [S16] D. Bohm and D. Pines, A collective description of electron interactions: III. coulomb interactions in a degenerate electron gas, *Phys. Rev.* **92**, 609 (1953).
- [S17] A. D. McLachlan and M. A. Ball, Time-dependent Hartree-Fock theory for molecules, *Rev. Mod. Phys.* **36**, 844 (1964).
- [S18] P. A. Dirac, The quantum theory of the emission and absorption of radiation, in *Proceedings of the Royal Society of London A: Mathematical, Physical and Engineering Sciences*, Vol. 114 (The Royal Society, 1927) pp. 243-265.
- [S19] F. Sottile, *Response functions of semiconductors and insulators: from the Bethe-Salpeter equation to time-dependent density functional theory*, Ph.D. thesis, Ecole Polytechnique X (2003).
- [S20] L. Hedin, New method for calculating the one-particle green's function with application to the electron-gas problem, *Phys. Rev.* **139**, A796 (1965).
- [S21] L. Hedin and S. Lundqvist, Solid state physics, Academic, New York **23**, 1 (1969).
- [S22] I.-K. Suh, H. Ohta, and Y. Waseda, High-temperature thermal expansion of six metallic elements measured by dilatation method and X-ray diffraction, *Journal of Materials Science* **23**, 757 (1988).
- [S23] Opium:the optimized pseudopotential interface unification module, <http://opium.sourceforge.net/>, accessed: 2017-11-30.
- [S24] P. Giannozzi, S. Baroni, N. Bonini, M. Calandra, R. Car, C. Cavazzoni, D. Ceresoli, G. L. Chiarotti, M. Cococcioni, I. Dabo, A. D. Corso, S. de Gironcoli, S. Fabris, G. Fratesi, R. Gebauer, U. Gerst-

- mann, C. Gougoussis, A. Kokalj, M. Lazzeri, L. Martin-Samos, N. Marzari, F. Mauri, R. Mazzarello, S. Paolini, A. Pasquarello, L. Paulatto, C. Sbraccia, S. Scandolo, G. Sclauzero, A. P. Seitsonen, A. Smogunov, P. Umari, and R. M. Wentzcovitch, Quantum espresso: a modular and open-source software project for quantum simulations of materials, *Journal of Physics: Condensed Matter* **21**, 395502 (2009).
- [S25] P. Giannozzi, O. Andreussi, T. Brumme, O. Bunau, M. B. Nardelli, M. Calandra, R. Car, C. Cavazzoni, D. Ceresoli, M. Cococcioni, N. Colonna, I. Carnimeo, A. D. Corso, S. de Gironcoli, P. Delugas, R. A. D. Jr, A. Ferretti, A. Floris, G. Fratesi, G. Fugallo, R. Gebauer, U. Gerstmann, F. Giustino, T. Gorni, J. Jia, M. Kawamura, H.-Y. Ko, A. Kokalj, E. Küçükbenli, M. Lazzeri, M. Marsili, N. Marzari, F. Mauri, N. L. Nguyen, H.-V. Nguyen, A. O. de-la Roza, L. Paulatto, S. Poncé, D. Rocca, R. Sabatini, B. Santra, M. Schlipf, A. P. Seitsonen, A. Smogunov, I. Timrov, T. Thonhauser, P. Umari, N. Vast, X. Wu, and S. Baroni, Advanced capabilities for materials modelling with quantum espresso, *Journal of Physics: Condensed Matter* **29**, 465901 (2017).
- [S26] N. Marzari, D. Vanderbilt, A. De Vita, and M. C. Payne, Thermal contraction and disordering of the Al(110) surface, *Phys. Rev. Lett.* **82**, 3296 (1999).
- [S27] H. J. Monkhorst and J. D. Pack, Special points for brillouin-zone integrations, *Phys. Rev. B* **13**, 5188 (1976).
- [S28] Thermo-pw:Ab-initio computation of material properties, https://dalcorso.github.io/thermo_pw/, accessed: 18.09.2019.
- [S29] O. K. Orhan and D. D. O'Regan, Plasmonic performance of $\text{Au}_x\text{Ag}_y\text{Cu}_{1-x-y}$ alloys from many-body perturbation theory, *Journal of Physics: Condensed Matter* **31**, 315901 (2019).
- [S30] A. Marini, C. Hogan, M. Grüning, and D. Varsano, yambo: An ab initio tool for excited state calculations, *Computer Physics Communications* **180**, 1392 (2009).
- [S31] T. Rangel, M. Del Ben, D. Varsano, G. Antonius, F. Bruneval, F. H. da Jornada, M. J. van Setten, O. K. Orhan, D. D. O'Regan, A. Canning, A. Ferretti, A. Marini, G.-M. Rignanese, J. Deslippe, S. G. Louie, and J. B. Neaton, Reproducibility in G_0W_0 calculations for solids, *Computer Physics Communications* **255**, 107242 (2020).